Aseismic Fault Slip during a Shallow Normal-Faulting Seismic Swarm Constrained Using a Physically-Informed Geodetic Inversion Method

Yu Jiang[1], Sergey Samsonov[2], and Pablo J González[1]

[1]University of Liverpool
[2]Natural Resources Canada

November 30, 2022

Abstract

Improved imaging of the spatio-temporal growth of fault slip is crucial for understanding driving mechanisms of earthquakes and faulting. This is especially critical to properly evaluate the evolution of seismic swarms and earthquake precursory phenomena. Fault slip inversion is an ill-posed problem and hence regularization is required to obtain stable and interpretable solutions. An analysis of compiled finite fault slip models shows that slip distributions can be approximated with a generic elliptical shape, particularly well for M[?]7.5 events. Therefore, we introduce a new physically-informed regularization to constrain the spatial pattern of fault slip distribution. Our approach adapts a crack model derived from mechanical laboratory experiments and extends it to allow for complex slipping patterns by stacking multiple cracks. The new inversion method successfully recovered different simulated time-dependent patterns of slip propagation, i.e., crack-like and pulse-like ruptures, directly using wrapped InSAR phase observations. We find that the new method reduces model parameter space, and favors simpler interpretable spatio-temporal fault slip distributions. We apply the proposed method to the 2011 March-September normal-faulting seismic swarm at Hawthorne (Nevada, USA), by computing ENVISAT and RADARSAT-2 interferograms to estimate the spatio-temporal evolution of fault slip distribution. The results show that (1) aseismic slip might play a significant role during the initial stage, and (2) this shallow seismic swarm had slip rates consistent with those of slow earthquake processes. The newly proposed method will be useful in retrieving time-dependent fault slip evolution, and is expected to be widely applicable to study fault mechanics, particularly in slow earthquakes.

Aseismic Fault Slip during a Shallow Normal-Faulting Seismic Swarm Constrained Using a Physically-Informed Geodetic Inversion Method

Yu Jiang[1], Sergey V. Samsonov[2], and Pablo J. González[1,3]

[1]COMET, Dept. Earth, Ocean and Ecological Sciences, School of Environmental Sciences, University of Liverpool, Liverpool, L69 3BX, United Kingdom

[2]Canada Centre for Mapping and Earth Observation, Natural Resources Canada, 560 Rochester Street, Ottawa, ON K1S5K2, Canada

[3]Department of Life and Earth Sciences, Instituto de Productos Naturales y Agrobiología (IPNA-CSIC), 38206 La Laguna, Tenerife, Canary Islands, Spain

Key Points:

- We estimate time-dependent fault slip to interpret geodetic data (wrapped phase InSAR) by adapting an experimental laboratory-derived model.
- The 2011 Hawthorne shallow seismic swarm migrated from south to north, initiated as aseismic slip preceding the most energetic event M4.6.
- Slip evolution shares similar slip rates with other slow-slip phenomena, implying that aseismic processes play a notable role during swarms.

Corresponding author: Yu Jiang, `Yu.Jiang@liverpool.ac.uk`

Abstract

Improved imaging of the spatio-temporal growth of fault slip is crucial for understanding driving mechanisms of earthquakes and faulting. This is especially critical to properly evaluate the evolution of seismic swarms and earthquake precursory phenomena. Fault slip inversion is an ill-posed problem and hence regularization is required to obtain stable and interpretable solutions. An analysis of compiled finite fault slip models shows that slip distributions can be approximated with a generic elliptical shape, particularly well for M$\leq$7.5 events. Therefore, we introduce a new physically-informed regularization to constrain the spatial pattern of fault slip distribution. Our approach adapts a crack model derived from mechanical laboratory experiments and extends it to allow for complex slipping patterns by stacking multiple cracks. The new inversion method successfully recovered different simulated time-dependent patterns of slip propagation, i.e., crack-like and pulse-like ruptures, directly using wrapped InSAR phase observations. We find that the new method reduces model parameter space, and favors simpler interpretable spatio-temporal fault slip distributions. We apply the proposed method to the 2011 March-September normal-faulting seismic swarm at Hawthorne (Nevada, USA), by computing ENVISAT and RADARSAT-2 interferograms to estimate the spatio-temporal evolution of fault slip distribution. The results show that (1) aseismic slip might play a significant role during the initial stage, and (2) this shallow seismic swarm had slip rates consistent with those of slow earthquake processes. The newly proposed method will be useful in retrieving time-dependent fault slip evolution, and is expected to be widely applicable to study fault mechanics, particularly in slow earthquakes.

Plain Language Summary

A key earthquake science challenge is to understand when an instability on a fault will arrest or run away into a large rupture. However, the slip nucleation process seems not to produce seismic waves and hence remains hidden to most seismological methods. Geodetic methods, which can directly measure motions at earth's surface, offer a complementary tool to improve our ability to map the fault slip. In this work, we expand an experimentally observed crack model, and propose a new inversion method for finding models of fault slip that can fit the observations of surface motions. The new method greatly reduces computation complexity respecting previous state-of-the-art methods, and is validated against synthetic experiments. We apply this new method to 2011 Hawthorne earthquake swarm (Nevada, USA), and discovered an aseismic slow slip before seismicity rate increased. That preparation stage was followed by a triggered larger slip on a nearby fault, and after that, the seismicity and fault slip rate reduced rapidly. We expect that this new methodology will be applied to detect similar precursory aseismic slip during long-lasting earthquake sequences, and allow us to retrieve detailed slip growth in space and time, which ultimately will advance our understanding of the faulting mechanics.

1 Introduction

How fault slip nucleates, grows and eventually accelerates is a critical question to describe the driving mechanisms behind earthquakes and faulting phenomena. Our current understanding is consistent with various mechanisms to initiate fault slip: dynamic triggering (Gomberg & Johnson, 2005), tidal triggering (Delorey et al., 2017), pore-pressure diffusion (Parotidis et al., 2003) or aseismic slip (Radiguet et al., 2016; Gualandi et al., 2017; Caballero et al., 2021). In particular, Gomberg (2018) summarized two leading hypotheses for earthquake nucleation. One proposes a stochastic model in which each earthquake triggers subsequent ones in a cascade fashion, while the other favors a deterministic view where slow-slip triggers and precedes the occurrence of a seismically dynamic rupture. Within the scope of distinguishing between the two earthquake nucleation models, one opportunity is to increase our ability to image how fault slip evolves in space and time. Although fault slip evolution is not necessarily the only cause of seismicity migrating, it may provide crucial data to examine various hypotheses for earthquake nucleation mechanisms.

Fault slip propagation has characteristics that permit discriminating between regular earthquakes and slow-slip phenomena, such as slip rate. For regular earthquakes, the peak and average slip rate are of the order of 1 m/s and 0.1 m/s (Takenaka & Fujii, 2008). For slow-slip phenomena, slip rates are much lower, e.g., Slow Slip Events (SSEs), fault creep, or slip related to fluid injection. The range of peak slip rate in SSEs on subduction zones is 0.1∼3 cm/day (Radiguet et al., 2011; Bletery & Nocquet, 2020; Rousset et al., 2019; Ozawa et al., 2019), whereas the fast slip rate in episodic creep events on the continental faults are 0.5∼3 cm/year (Schmidt et al., 2005; Jolivet et al., 2012; Hussain et al., 2016; Scott et al., 2020). In fluid injection experiments, the slip rate has been observed to be much higher, up to 4×10^{-3} mm/s (35 cm/day) (Guglielmi et al., 2015).

To evaluate fault slip characteristics, a better description of how fault slip propagates in space and time is necessary. Two propagation patterns of seismic rupture were described in Lambert et al. (2021) and Marone and Richardson (2006): pulse-like and crack-like ruptures. The two distinguishable patterns are also observed in slow-slip phenomena: slow slip could either migrate further and further away from where it started along strike (or dip), or stay almost stationary through time. Observations of some SSEs and "Episodic Tremor and Slip" (ETS) show that they are pulse-like ruptures with elongated slipping areas on some subductions zones and follow the first pattern, e.g., the Cascadia subduction zone (Michel et al., 2019). For the migration along strike, the migration speed is ∼10 km/day (Wech et al., 2009; Rousset et al., 2019). In contrast, slip propagation in the meter-scale fluid injection experiment follows the second pattern. Bhattacharya and Viesca (2019) proposed a model in which the slip grows like expanding ellipses, with the injection point as the slipping center. The latter phenomenon is also found in some SSEs on subduction zones, e.g., the deeper Manawatu and Kaimanawa SSEs on the Hikurangi subduction zone (Wallace, 2020).

In this research, we developed a new method to interpret directly wrapped phase InSAR observations to estimate the spatio-temporal fault slip, in particular, in the context of continental seismic swarms (e.g., small-amplitude surface deformation signals and/or phase discontinuities due to surface ruptures). InSAR has been used to map surface displacements with high spatial resolution and subsequently model fault slip. But so far, it is more common to estimate static slip distributions than jointly invert for the time-series of slip evolution (Floyd et al., 2016; Ingleby et al., 2020). The problem of retrieving time series of source parameters from non-simultaneous and temporally overlapped multi-sensor observations is ill-posed; however, the oscillations of the solution caused by the rank deficiency of this problem can be reduced by applying regularization or temporal filtering (Samsonov & D'Oreye, 2012). Grandin et al. (2010) introduced a temporal smoothing scheme as an additional constraint to retrieve the time series of magma volume changes. Additionally, González et al. (2013) used truncated singular value decomposition (TSVD) to reject model space basis vectors associated with small singular values. Instead of regularizing the volume variation itself, they minimized the volume change rate, to avoid large discontinuities. Here, we improve previous methods by a) regularizing the fault slip distribution using a prescribed parametrization derived from a laboratory-based crack model, and b) introducing a statistically optimal truncation criterion that allows to automatically separate signal and noise in the spatio-temporal fault slip distributions. We demonstrated the validity of this approach using synthetic experiments and comparing it against a compilation of published slip distribution models. Finally, we applied the new proposed methodology to the 2011 Hawthorne seismic swarm (Nevada, USA). The 2011 Hawthorne seismic swarm is located at the central Walker Lane, which accommodates the Pacific-North American transform plate motion by oblique-normal faults and block rotations. The 2011 Hawthorne swarm consists of 10 M4+ events, and the largest earthquake among them is a M4.6 event (Zha et al., 2019; Smith et al., 2011); recent study using satellite images reveals clear surface deformation signals before the M4.6 event, and the geodetic moment is much higher than the seismic moment, indicating that aseismic slip dominates the fault behavior (Jiang & González, 2021). By applying our newly proposed methodology, we retrieved the fault-slip spatio-temporal evolution, and the results will help us to better understand the fault mechanics and seismic hazard in Walker Lane.

2 Time-Dependent Fault Slip Inferred Using Geodetic Fault Slip Models

2.1 Static Fault Slip Models

Slip inversions with kinematic models are ill-posed problems in which the solution is nonunique and unstable, and unphysical slip distributions can be estimated by Least-Square algorithms, i.e., extremely rough oscillatory slip distributions. Harris and Segall (1987) introduced Laplacian smoothing as the regularization scheme. This minimizes the second derivative of slip and can prevent cases with large stress drops. Du et al. (1992) plotted a trade-off curve for misfit as a function of slip roughness, and manually picked a smoothing factor within the inflection point of the curve to find an optimal balance between data fit and model roughness. Matthews and Segall (1993) determined the optimal smoothing factor in the trade-off curve objectively by implementing the cross-validation method. Much later, Fukahata and Wright (2008) and Fukuda and Johnson (2008) introduced the Bayesian approach, ABIC (Akaike's Bayesian Information Criterion), to solve the slip distribution. While Fukahata and Wright (2008) emphasized the significance of fault geometry as a nonlinear constraint, Fukuda and Johnson (2008) overcame the deficiencies of ABIC with positivity constraints, and then applied the adapted ABIC to simultaneously estimate the slip distribution and smoothing parameter objectively in a Bayesian framework. Fukuda and Johnson (2010) then devised a mixed linear-non-linear Bayesian inverse formulation and extended their work for the joint slip and geometry inversion. In response, Minson et al. (2013) argued that the non-physical regularization scheme (i.e., Laplacian smoothing) is unnecessary, and developed a fully Bayesian approach to sample all possible families of models compatible with the observations, via a parallel computing framework. Ragon et al. (2018) further extended the work of Minson et al. (2013) and accounted for the uncertainty in fault geometry. Instead of Laplacian regularization, Amey et al. (2018) developed an inversion package *slipBERI*, and incorporated self-similarity, characterizing the seismic slip distribution in real earthquakes, as a prior assumption within the Bayesian inversion of earthquake slip.

All the previous methods are based on kinematic models that do not take into account the relationship between stress and slip in the fault. Alternatively, dynamic source models satisfy physical constraints on the propagation of shear fractures on Earth, but few dynamic source models are considered to constrain the slip inversions. As an alternative, Di Carli et al. (2010) proposed using elliptical patches to describe the slip distribution in the kinematic and dynamic inversion of near-field strong motion data at low frequencies. Soon afterward, Sun et al. (2011) put forward a *mechanical* slip inversion, imposing a uniform stress drop on the fault plane. The resulting slip distribution is inherently smooth, so the smoothing norm and the smoothing factor are unnecessary. Tridon et al. (2016) assumed a circular stress patch in volcano research, inverting the displacement for shear and normal stresses simultaneously, along with the fault geometry.

In this study, we present a Geodetic fault-slip Inversion using a physics-based Crack Model (GICMo), developed and demonstrated by Jiang et al. (2021). A one-dimensional analytical crack model is proposed by Ke et al. (2020), and it fits experimental laboratory earthquake measurements of ruptures contained within a 3-meter-long saw-cut granite fault. This new crack model features non-singular (finite) peak stresses at the rupture tip. Jiang et al. (2021) expanded the one-dimensional model into two-dimensional within an elliptical shape, by assuming one of the focal points of the ellipse to be the crack center (with the maximum slip) and the elliptical perimeter to be the crack tip. Therefore, the slip distribution on the fault plane is controlled by a very compact and reduced set of parameters. The geodetic-inverted fault slip infers that it is possible that the crack center can be located at the rupture center, e.g., 2009 L'Aquila earthquake (Walters et al., 2009). So we relax the constraint of the crack center location, and allow it to move along the x axis inside the ellipse. Our crack model contains only eight parameters as demonstrated by Equation 1 and Figure 1.

$$s = \mathbf{f}(x_0, y_0, a, e, \alpha, \lambda, d_{max}, \theta) \tag{1}$$

where s is the slip distribution; x_0, y_0 are the locations of the crack center; a and e are the semi-major axis and eccentricity of the ellipse; α is the ratio controlling the location of crack center along x axis: the crack center is located at the ellipse center, left/right vertices when $\alpha = 0, -1/1$; λ is the ratio controlling the displacement transition from the center to the edge of the elliptical crack; d_{max} is the maximum slip; θ is the rake angle.

In the GICMo method, once the crack model parameters are provided, the slips for all fault patches are then determined based on the two-dimensional crack model discussed above. Then, the fault slip distribution is forward modeled to estimate surface displacement. Following Jiang and González (2020), a misfit function is constructed based on the wrapped phase residuals and the weighting matrix. The misfit function is then regarded as the likelihood function fed into the Bayesian process to retrieve the posterior distribution of crack model parameters. In the Bayesian process, the Markov chain Monte Carlo algorithm is adopted as the probability sampling approach based on the Metropolis-Hasting rule.

Here we design a synthetic static slip to compare the performance of our method, GICMo, and a state-of-the-art method, slipBERI (Amey et al., 2018). The geodetic inversion package, slipBERI, solves for fault slip with GNSS and unwrapped InSAR phases in a Bayesian approach using von Karman regularization, and simultaneously solves for a hyperparameter that controls the degree of regularization. A normal fault with pure down-dip slip is simulated as the synthetic fault model. To imitate the slipping patterns observed in the published finite-source rupture models SRCMOD (Mai & Thingbaijam, 2014) (e.g., Bennett et al. (1995), Ichinose et al. (2003), and Elliott et al. (2010)), the inner region is a square area with a larger displacement, and the outer region is an annulus area with a smaller displacement (Figure 2). Due to the difference in the ingestion data, the synthetic phases are unwrapped phases for slipBERI and wrapped phases for GICMo. The displacement phase is forward calculated based on the synthetic fault slip distribution and the dislocation model. To increase its resemblance to reality, decorrelation and atmosphere noises are simulated and added, whose amplitudes are 10% of 2π for wrapped phase cases or the peak amplitude of the deformation phase for unwrapped phase cases, which is based on the signal-to-noise ratio from a real interferogram in Section 4 (RS2-20110322-20110415). The simulated noise-plus-deformation interferogram is resampled with a quadtree algorithm within the downsampled unwrapped and wrapped phases (Bagnardi & Hooper, 2018; Jiang & González, 2020). In addition, the covariance matrix is estimated based on the phase in the far-field. Finally, the downsampled phases and covariance matrix are fed into slipBERI and GICMo to retrieve the slip distributions. Figures 2b-2d show the modeled slip distribution inverted by GICMo and slipBERI, and Figure S1 shows the modeled phase and phase residuals. The conclusions are listed below.

(1) Both GICMo and slipBERI provide the first-order accuracy of the slip distribution, including the locations of the crack center and the magnitude of the slip peak.

(2) We interpolate the slip distribution onto a 0.5 km $\times$ 0.5 km patch mesh, and calculate the root-mean-square (RMS) of the slip distribution compared with the synthetic slip distribution. We find that the RMSs are 1.5 cm for one-ellipse model, 2 cm for von Karman smoothing model, and 3 cm for Laplacian smoothing model, which are approximately similar. However, the great advantage is that the parameters to be solved in GICMo are independent of the fault mesh discretization, and the number of parameters is 30 times less in this case than 201 in slipBERI for this case.

2.2 Bayesian Inversion of Fault Slip Time-Series Using a Physics-based Crack Model (Time-GICMo)

The temporal evolution of fault slip is critical to understanding the driving mechanism of slow slip. It is difficult to find one slow slip event where one interferogram can coincidentally capture the beginning and the ending of the activity. Instead, a common scenario is that the slip increment is captured by interferograms. In this section, we develop a new method of retrieving the slip increments and demonstrate the time-series slip estimation with synthetic experiments. Assuming two elliptical ruptures at the beginning and the ending, slip increment $\Delta s = s^2 - s^1$, where s^2 and s^1 are the slip distributions at the end and the beginning of the interferogram.

We consider a system of N increments of fault slip ($\Delta s^n \in [\Delta s^1, ..., \Delta s^N]$ between dates t_i^n and t_j^n) based on the non-linear inversion estimation from the corresponding wrapped interferogram, and the raw images of interferograms are acquired at M unique dates ($t \in [t_1, ..., t_M]$). The aim is to solve for the temporal evolution of fault slips ($s \in [s_1, ..., s_M]$) for each date. We assume that the slip rate between adjacent dates ($v_m \in [v_1, ..., v_{M-1}]$) are constant, so the slip increment Δs^n can be expressed by the sum of fault slip increment between adjacent dates, $\Delta s^n = \sum_{m=i}^{j-1} v_m (t_{m+1}^n - t_m^n)$. The linear expression for N increments of fault slip is shown in Equation 2, as illustrated by González et al. (2013):

$$
\begin{aligned}
\mathbf{P} &= \mathbf{BQ} \\
\mathbf{P} &= [\Delta s^1 \quad \cdots \quad \Delta s^n \quad \cdots \quad \Delta s^N]^T \\
\mathbf{Q} &= [v_1 \quad \cdots \quad v_m \quad \cdots \quad v_{M-1}]^T \\
\mathbf{B}(n,m) &= \begin{cases} t^n_{m+1} - t^n_m, & \text{if } i \leq m \leq j-1. \\ 0, & \text{otherwise.} \end{cases}
\end{aligned}
\tag{2}
$$

where $\mathbf{P}$ is the observation vector, $\mathbf{Q}$ the unknown vector, and $\mathbf{B}$ the designed matrix. Considering there are N increments of fault slip, the matrix dimension is $(N \times 1)$ for $\mathbf{P}$, $(N \times (M-1))$ for $\mathbf{B}$, and $((M-1) \times 1)$ for $\mathbf{Q}$. Then, we decompose matrix $\mathbf{B}$ by using the SVD methods,

$$\mathbf{B} = \mathbf{USV}^T \tag{3}$$

where $\mathbf{U}$ is an orthogonal matrix with columns that are the basis vectors of the data space $(N \times N)$, $\mathbf{V}$ is an orthogonal matrix with columns that are the basis vectors spanning the singular values of the model $((M-1) \times (M-1))$, and $\mathbf{S}$ is a diagonal matrix of the singular values $((N \times (M-1)) \times 1)$. A solution for this problem can be obtained as follows,

$$\mathbf{Q} = \mathbf{VS}^{-1}\mathbf{U}^T\mathbf{P} \tag{4}$$

If rank($\mathbf{B}$)<m, the solution obtained using the SVD technique may contain numerical instabilities when there are small singular values. In this case, a more stable solution can be achieved using the TSVD method (Aster et al., 2019), which rejects model space basis vectors associated with small singular values, up to a certain threshold. As an improvement on González et al. (2013), we apply an optimal hard threshold for singular values proposed by Gavish and Donoho (2014). Gavish and Donoho (2014) proposed that the optimal hard threshold for singular value is $4/\sqrt{3}$ of the median singular value. This criterion is empirically proven to be the best hard thresholding, independent of model size, noise level, or true rank of the low-rank model. This improvement allows us to define the degree of regularization based on objective criteria, which generates a low-rank model from noisy data. Note that in order to retrieve a realistic solution, a non-negative constraint is added in solving for slip rate vector Q implemented by using MATLAB function *lsqnonneg* (`https://uk.mathworks.com/help/optim/ug/lsqnonneg.html`). It is

physically appropriate because a fault is rarely observed to move backward, with only one known example (Hicks et al., 2020).

3 Time-dependent Fault Slip Inversion Experiments

In this section, we describe two experiments to simulate pulse-like and crack-like rupture propagation patterns in space and time. We tested the performance of the inversion method to recover fault slip evolution from each of the two-ellipse model.

The first synthetic case aims to explore the inversion with overlapping ruptures (Figure 3). A number of recent studies have suggested spatial overlap between coseismic slip and afterslip (Barnhart et al., 2016; Bedford et al., 2013; Bürgmann et al., 2002; Johnson et al., 2012; Pritchard & Simons, 2006; Salman et al., 2017; Tsang et al., 2016). A series of overlapping elliptical cracks are simulated in Figure 3a, and a forward inversion is performed to calculate the surface displacement due to the slip increment between adjacent cracks. We aimed to compare the results based on various geodetic inversion algorithms: (1) the one-ellipse model, as described in Section 2.1, (2) a von Karman regularization algorithm (Amey et al., 2018), (3) the two-ellipse model with different crack centers. Inversions results are shown in Figures 3b-3d, and the modeled phase and residuals are shown in Figures S2-S3. The main conclusions are as follows.

(1) The RMS of the fault slip residual is the lowest in results based on the two-ellipse model with different centers. The triangle patch size in the crack model is $\sim$0.84 km, and the rectangle patch size in slipBERI is 1.5 km. In this way, we interpolated the modeled slip distributions to grid points with 1.17 km spacing, and then calculated the RMS of the fault slip residual. In each case, the RMS of slip residuals based on the two-ellipse model with different centers (Figure 3d) are the smallest, and the average RMS for one-ellipse model, von Karman smoothing model and the two-ellipse model are 0.9 cm, 1.6 cm, and 0.6 cm.

(2) The two-ellipse model is superior to the one-ellipse model in the F-test for the residual of the interferometric phase. The two-ellipse model has more free parameters, leading to an inherent improvement in the data fit. To objectively compare the model performances, we use F-ratio statistic to test the significance of decrease of residuals between models (Stein & Gordon, 1984). The statistical test checks if the empirical F-ratio (F_{emp}) is larger than the theoretical (F_{theory}). In this case, the comparison of the one-ellipse model and two-ellipse model leads to $F_{emp} = 72.8 \gg F_{theory} = 2.6$.

The second synthetic case aims to explore the inversion with the containing ruptures (Figure 4). A growing rupture has been widely observed and studied in fluid injection experiments (Guglielmi et al., 2015; Bhattacharya & Viesca, 2019; Cappa et al., 2019). The rupture center is located at the injection point, and the radius of the slipping zone grows at a rate up to 10^{-6} m/s. A set containing elliptical ruptures is simulated in Figure 4a, and a forward inversion facilitates the surface displacement calculation. We aimed to retrieve the slip increments from the observed interferometric phase with various methods described above (one-ellipse model, von Karman smoothing model, and two-ellipse model). On noticing that the slip distribution is not well resolved by the two-ellipse model with different centers, we added another constraint to the two-ellipse model so that both cracks share the same center. The inversion results are shown in Figures 4b-4e, and the modeled phase and residuals are shown in Figures S4-S5. The main conclusions are as follows.

(1) The average RMS of slip residuals based on various inversion models (one-ellipse model, von Karman smoothing model, two-ellipse model with different centers, and one center) are 1.3 cm, 1.3 cm, 1.0 cm, and 0.8 cm. The one-ellipse model failed because the slip increment in containing ruptures no longer could be described by one complete crack. Indeed, slipBERI showed better performance because it inferred the region with the slip peak. The two-ellipse model with different centers is even better but was not well resolved, e.g., the slip increment from t_1 to t_2 (second image in Figure 4c). Therefore, the two-ellipse model with the *same* center is the most appropriate in reconstructing the cracks' locations, sizes, and maximum slips.

(2) In the F-test of the interferometric phase residuals, the two-ellipse model with the same center is superior to the two-ellipse model with different centers, and the one-ellipse model is the least useful model.

4 Application case: the 2011 Hawthorne Seismic Swarm (Nevada, USA)

4.1 Regional Tectonics and Seismicity

In this study, we focus on the 2011 Hawthorne seismic swarm, which occurred on the central Walker Lane (Figure 5). The Walker Lane is a 500 km-long and 100 km-wide deformation region consisting of N-NW right-lateral shear and extension (Wesnousky, 2005). It is located between the northwest translating Sierra Nevada microplate and the westward extending Basin and Range Province. The Walker Lane accommodates 20%

$\sim$ 25% of the current relative motion (50mm/year) between the Pacific and North American plates (Argus & Gordon, 1991; Faulds & Henry, 2008). The central Walker Lane accommodates the deformation budget of $\sim$8 mm/year between the Basin and Range province and the central Sierra Nevada (Bormann et al., 2016). The distributed dextral shear in central Walker Lane is accommodated by oblique-normal faults, block rotations, and partitioning of oblique deformation between sub-parallel normal and strike-slip faults. The total long-term strain rate is 51 nanostrain/year extension directed N77°W and 38 nanostrain/year contraction directed N13°E (Kreemer et al., 2014), much higher than the central Basin and Range (Kreemer et al., 2009).

Being a geologically young and developing fault system, the Walker Lane underwent long-lasting seismicity over the instrument period, including >10 M6+ earthquakes in the last century, and it is regarded as a natural laboratory to study seismicity and fault mechanics and to evaluate the seismic hazard in Southern California (Wesnousky, 2021). A few seismic sequences struck the Walker Lane since 2000, e.g., the 2008 Mogul earthquake sequence (Ruhl et al., 2016, 2017), the 2011 and 2016 Hawthorne seismic swarm (Smith et al., 2011), the 2017 Truckee sequence (Hatch et al., 2018), the 2014 Virginia City Swarm (Hatch et al., 2020), the 2016 Nine Mile Ranch sequence (Hatch, 2020), the 2020 Monte Cristo Range sequence (Ruhl et al., 2021). The 2011 Hawthorne seismic swarm lasted from March to September and consisted of 10 M4+ earthquakes according to the U.S. Geological Survey (USGS) hypocentre catalog (`https://earthquake.usgs.gov/earthquakes/search/`). This sequence occurred in the footwall block of the Wassuk Range segment at the central Walker Lane (Faulds & Henry, 2008), and this segment experiences a significant extension of 1.5±0.3 mm/year (Hammond & Thatcher, 2007). Early moment tensor solutions show the shallow depths in this sequence (Smith et al., 2011), and further hypocenter relocation together with the focal mechanisms of the M4+ events consistently reveal a W-NW-dipping normal fault zone with centroid depths between 2 km and 4 km (Zha et al., 2019). The 2011 Hawthorne sequence is close to the Aurora-Bodie volcano (Lange & Carmichael, 1996), but no volcanic signature was observed in near-source seismograms, which infers this sequence is not likely related to the magmatic activity (Smith et al., 2011; Zha et al., 2019). In this research, we identify three stages with respect to the time when the most energetic event (M4.6) occurred: an initial stage (pre-M4.6 stage) from 15 March to 17 April, the most energetic stage (co-M4.6 stage), and the post-energetic stage (post-M4.6 stage) until 17 September.

4.2 Multi-satellite Geodetic Datasets

We processed ENVISAT and RADARSAT-2 data and generated 8 SAR interferograms to quantify surface displacements (Figure 6). SAR images were acquired between February and September 2011 from two tracks: one ascending track from the Canadian Space Agency RADARSAT-2 satellite, look angle 35° and heading angle 350°; and another descending track from the European Space Agency (ESA) ENVISAT satellite, track 343, look angle 35° and heading angle -166°. Interferograms were processed in two-pass differential mode, using a 30m resolution digital elevation model (DEM) derived from the Shuttle Radar Topography Mission. ENVISAT-ASAR data were processed using Doris software (Kampes et al., 2003) and ISCE software, RADARSAT-2 data using GAMMA software (Werner, 2000). Overall, we obtained 8 short baseline differential interferograms. The computed interferograms have temporal separations ranging from 24 to 120 days. Considering the dominant extensional mechanism and N-S fault striking in this region, the preferred movement direction of the ground displacement is E-W. Consequently, the satellite flight direction favors surface displacement observations in this normal faulting system.

Interestingly, 2 ascending RADARSAT-2 interferograms during the pre-M4.6 stage indicated clear surface displacement signals (Figures 6d and 6a), ∼4 cm away from satellite line-of-sight motion. In interferograms covering the co-M4.6 stage, it is notable that surface displacement signals were larger in magnitude and located further north with respect to the pre-M4.6 stage (Figures 6b, 6c, 6e and 6f). During the early post-M4.6 stage, surface displacements were detected along a very narrow spatial band with clear phase discontinuities, suggesting surface ruptures (Figure 6g). For one interferogram covering the late post-M4.6 stage (Figure 6h), the phase was dominated by atmospheric noise and no clear deformation signal was detected. Analysis of interferograms suggests that fault slip may have occurred along a fault system with a two-plane geometry, which is consistent with the finding from early moment tensor solutions (Smith et al., 2011).

4.3 Spatio-temporal Slip Evolution

To develop the kinematic fault model, we first constructed the fault geometry by applying a state-of-the-art inversion method, solving for uniform distribution on rectangular faults (Jiang & González, 2020). The geodetic inversion is directly using the interferometric wrapped phase to avoid any potential phase unwrapping error (Figure S6). The data variance-covariances describing the noise level are calculated based on the covariograms (Figure S7) and are used to weight the wrapped phase residuals in the likelihood function as illustrated by Jiang and González (2020). Modeling of a selection of interferograms covering the successive phases confirmed that ground motion could be caused by fault geometry with two distinct planes. During the pre-M4.6 stage, the observed ground motion in the RADARSAT-2 interferogram (2011/03/22-2011/04/15, Figure 6d, and fault-normal profile in Figure 7d) would be consistent with slip along a N-S striking normal fault to the south (green rectangular fault in Figure 7a). After modeling the interferogram covering the co- and post-M4.6 stages (2011/04/15-2011/06/26, Figure 6f, and fault-normal profile in Figure 7c), Figure 6f shows a different fault segment on a NE-SW trending normal fault to the north (yellow rectangular fault in Figure 7a). Based on modeled fault geometry in Figure 7a, together with ground motion discontinuities digitized from the interferograms, we constructed a smooth fault plane with uniformly discretized triangular meshes in Figure 7d. These were generated by FaultResampler (Barnhart & Lohman, 2010) and mesh2d (Engwirda, 2014), with a near-uniform side length around 125 m. Then, a fault slip distribution model with associated uncertainties was estimated. We applied our newly developed fault slip inversion method, GICMo, based on a prescribed regularization derived from an experimentally validated physics-based crack model (Jiang et al., 2021). To further investigate the temporal evolution of fault slips with a higher temporal resolution, we invert the fault slip time-series using all available interferograms with clear deformation signals.

Figure 8 presents the temporal evolution of cumulative slip and slip rate during the 2011 Hawthorne seismic swarm, and Figure S9 shows the modeled phase and phase residuals. The findings from the inversion results are listed as follows.

(1) There were three areas with different spatio-temporal slipping behaviors: a narrow (5 km^2) slip area on the southern fault with a high rate (lower boundary: 1.5 cm/day, or 1.7×10^{-7} m/s) occurring during the pre-M4.6 stage, a wider (15 km^2) slip area with lower average slip (10 cm) on the northern fault that ruptured during the co-M4.6 stage, and a shallow slip area (depth=1 km) just above the second area during the post-M4.6 stage with a slower average slip rate (lower boundary: 0.2 cm/day, or 2.3×10^{-8} m/s).

(2) Our results show the aseismic slip mainly occurred on the southern subfault during the pre-M4.6 stage, while the most significant seismic slip hit the northern subfault

during the co- and post-M4.6 stages. The results are more consistent with a cascade model of discrete slip patches, rather than a slow-slip model considered as a growing elliptical crack.

(3) During the early pre-M4.6 stage (February 26-March 22), the cumulative geodetic moment is 1.7×10^{16} Nm (equivalent to a M_w 4.7 event), 45 times as large as the cumulative seismic moment (0.04×10^{16} Nm). The cumulative geodetic/seismic moment ratio reduces over time, but remains larger than 3 during the co- and post-M4.6 stages.

5 Discussion

5.1 On the Spatial Complexity of Fault Slip Distributions

Fault slip most likely has nonuniform spatial distribution due to spatial heterogeneities of rock strength and stress state on the fault, with well-known dependence on depth and the less understood along-strike variations. Seismic and geodetic inversions can reveal how fault slip is distributed on the discretized fault plane. However, to explore all possible models consistent with observations, the parameter space scales up rapidly to a large number of unknowns, increasing the problem's null-space, which means there are many vectors in the model space that are unconstrained by the data. Therefore, it is reasonable to consider our understanding of the complexity of slip distribution in natural earthquakes. The reasonable approach is able to allow for fault-slip heterogeneity, while keeping the problem null-space as small as possible. Mai and Beroza (2002) compiled published finite-source rupture models, and proposed the fractal pattern in slip distributions. It is true for large earthquakes, and multiple fault segments with several rupturing centers are revealed by geodetic and seismological observations, e.g., 2008 M_w7.9 Wenchuan earthquake (Shen et al., 2009), and 2016 M_w7.8 Kaikoura earthquake (Hamling et al., 2017). However, solving a huge number of parameters has a high computation cost. Computation complexities in their algorithms depend greatly on the number of discretized fault patches. For example, when studying a 40 km-long and 20 km-wide fault with slipBERI, there are 200 patches if the patch size is 2 km and the parameter' dimensions are 400. The latter would rapidly increase to 1600 if the patch size is 1 km. This is possibly the reason why the number of imported fault patches has upper bounds in practice, particularly if a Bayesian sampling strategy is employed. Though techniques like parallel computing have been introduced to improve computation efficiency, sampling such high-dimensional problems is still computationally challenging and does not solve the size of the null-space.

In this research effort, we favored a method that dramatically reduces the number of free parameters to solve; the drawback is that it results in *compact* fault slip distributions. However, our inverted slip distribution patterns are supported by the observations. This is a reasonable approach, because many inversion results support fault-slip distributions that are spatially compact, especially for small-magnitude earthquakes (Taymaz et al., 2007; Barnhart et al., 2014; Xu et al., 2016; Champenois et al., 2017; Ainscoe et al., 2017). Many studies have successfully modeled the majority of surface displacement signals using only one single fault with uniform distribution (Biggs et al., 2006; Nissen et al., 2007; Walters et al., 2009). For slow slip events across the global subduction zones, distribution patterns usually follow an elliptical shape with one slipping center (Wallace et al., 2012; Villegas-Lanza et al., 2016; Fukuda, 2018), and the fractal pattern is not required.

Benefiting from the online database of finite fault rupture models, SRCMOD (Mai & Thingbaijam, 2014), we were able to quantitatively evaluate how well a single elliptical model fits the available slip distributions across various tectonic settings and magnitudes. We retrieved 300 slip distributions on a single fault from SRCMOD, and intended to model the slip distributions with the one-ellipse model. Our experiments showed that for 85% of $M_w \leq 7.5$ events, the RMS of the slip residual is less than 20% of the peak slip (Figure S10). In addition, a simple circular crack is also the widely accepted assumed model in stress drop estimation based on seismic spectra (Madariaga, 1976; Kaneko & Shearer, 2014). Though only small degrees of freedom is allowed in the one-ellipse model, complexity could be added by incorporating multiple ruptures. As we showed in Section 2.2, a half-moon pattern was retrieved by two containing or overlapping elliptical crack models. Similarly, it is possible to overlap multiple ruptures to simulate multiple peak slips or more complex patterns.

The compact slip distribution in this new elliptical model is also favorable to evaluate the statistics of small earthquakes. Earthquake source parameters characterization of small earthquakes is important for understanding the physics of source processes and might be useful for earthquake forecasting (Uchide et al., 2014). A wide-used source model to analyze the source parameters of small earthquakes is a circular crack rupture (Brune, 1970; Madariaga, 1976) with stress singularity at the crack tip, and we hope our new elliptical slip model, which avoids this stress singularly, can be an alternative source model in the future (Shearer et al., 2006). Furthermore, by taking advantage of the improved method for estimating slip rates during temporally overlapping InSAR timeframes, one can image the fault behavior over a long period in a relatively high temporal resolution. This new method is expected to be applied to investigate the temporal evolution of slow fault slip, e.g., transient slow slip (Khoshmanesh et al., 2015; Kyriakopoulos et al., 2013; Klein et al., 2018), afterslip (Thomas et al., 2014), and slow slip events in subduction zones (Bletery & Nocquet, 2020; Rousset et al., 2019; Ozawa et al., 2019).

5.2 Time-dependent Fault Kinematics during Continental Seismic Swarms and Other Slow Earthquakes

During the initial stage of the 2011 Hawthorne seismic swarm, a substantial amount of aseismic slip ruptured on the southern subfault without strong seismicity (e.g., the first two periods in Figure 8b), with peak slip rates of 1.1∼5.4 cm/day, average slip rate 0.4∼1.9 cm/day and migration velocity 0.05 km/day. The phenomena potentially driven by aseismic slip are widely explored, e.g., ETS, Rapid Tremor Reversals (RTRs), SSEs, fault creep, and fluid injection. To better compare this precursory aseismic slip with other identified phenomena in the slow slip family, we compile the slip rates and migration velocities found in the literature list below and in Table S1.

(1) The peak slip rate. SSEs show a wide range of peak slip rate among subduction zones, e.g., 0.27 cm/day for Cascadia subduction zone (Bletery & Nocquet, 2020), 0.3 cm/day for South Central Alaska Megathrust (Rousset et al., 2019), 0.6∼2.8 cm/day for Japan trench (Hirose & Obara, 2010; Ozawa et al., 2019). During the early stage of the 2011 Peloponnese seismic swarm (Greece) (Kyriakopoulos et al., 2013), the fault behavior was dominated by aseismic slip inferred from the geodetic and seismic moment, and the peak slip rate was 0.26 cm/day. The maximum slip rate in fault creep events are very low, e.g., 0.5 cm/year on the Hayward fault (Schmidt et al., 2005), 0.5 cm/year on the Haiyuan Fault (Jolivet et al., 2012; Song et al., 2019), 0.8 cm/year on the North Anatolia Fault (Hussain et al., 2016) and 3 cm/year on the San Andreas Fault (Johanson & Bürgmann, 2005; Khoshmanesh et al., 2015; Scott et al., 2020). However, in the fluid injection experiment the slow aseismic slip during the early stage was much higher, 4×10^{-3} mm/s (35 cm/day) (Guglielmi et al., 2015), potentially because the measurement

in the fluid injection is real-time, and the duration uncertainty is much lower than SSEs observations.

(2) The average rate of slip increment. Research on the 2010-2014 seismic swarm in southern Italy (Cheloni et al., 2017) is consistent with our findings. This research revealed that the average slip rate started to increase two months before the largest shock (M_w5.1) and reached the highest value, ∼0.1 cm/day, a few days before the largest shock. It then decreased to zero in the following months. This highest average slip rate was at the same level with ∼0.4-1.9 cm/day in our research. The aseismic slip rate inferred by RE is much lower, ∼0.3-3 cm/year (Nadeau & McEvilly, 1999; Turner et al., 2013; Mesimeri & Karakostas, 2018).

(3) Migration velocity. These velocities of ETS and SSEs vary with subduction zones (Yamashita et al., 2015), but the generally reported migration velocity along the strike of the plate geometry is ∼10 km/day (Wech et al., 2009; Wallace et al., 2012), while RTRs propagate 'backward' 20 to 40 times faster than ETS advances forward (Houston et al., 2011). The large-scale features of ETS propagation with RTRs are reproduced and supported by numerical experiments (Luo & Liu, 2019; Liu et al., 2020). Similarly, migration velocity in TES varies over a wide range, from 0.5 to 14 km/day (Passarelli et al., 2018; De Barros et al., 2020).

5.3 Spatially variable mechanical response of the Hawthorne swarm faults

As shown in Figure 8b, the southern segment is active during the pre-M4.6 stage, and the fault behavior is mostly dominated by aseismic slip, inferred from a very high geodetic/seismic moment ratio $\in [25, +\infty]$ (Figure 8c), while the general cumulative geodetic/seismic moment ratio remains larger than three for the whole seismic swarm. This significant portion of aseismic slip identified here has been reported associated with a handful of continental seismic swarms (Lohman & McGuire, 2007; Wicks et al., 2011; Kyriakopoulos et al., 2013; Gualandi et al., 2017; Cheloni et al., 2017). In 2005, a tectonic swarm of over a thousand earthquakes occurred in the Salton Trough, California (USA) and Lohman and McGuire (2007) revealed the geodetic moment of the modeled fault system was about seven times the cumulative seismic moment of the swarm. Wicks et al. (2011) studied a swarm in southeastern Washington (USA) and also found the geodetic/seismic moment ratio was about seven. During the 2011 Peloponnese Penisula seismic swarm (Greece), Kyriakopoulos et al. (2013) revealed a big discrepancy of moment release, where the geodetic moment was ∼5 times the cumulative seismic moment for the interval July 3-October 1. For the 2013-2014 Northern Apennines seismic swarm (Italy), the moment associated with aseismic deformation/the seismic moment ratio is between 70% ± 29% and 200% ± 70% (Gualandi et al., 2017). For the 2010-2014 Pollino seismic swarm (Italy), Cheloni et al. (2017) found 70% of the moment was released aseismically. Above all, though it is possible that the estimated geodetic moment could be biased by the noise in the data or the inversion method, it cannot rule out that the significant portion of seismic swarms are accompanied by aseismic slip, in the light of the estimated ratios between the geodetic moment and seismic moment reaching high values, such as ∼5-8. Furthermore, the compact fault slip identified during the pre-M4.6 stage is favored by our improved methodology as demonstrated in Section 2. The previous finding of fractal distribution of fault slip is based on M5.9+ earthquakes (Mai & Beroza, 2002), while small-to-moderate-magnitude ruptures would have more compact slip distribution with low complexity as observed in the rupture models SRCMOD (Mai & Thingbaijam, 2014). Therefore, we hope that our improved method can be used to improve the detection of similar small-to-moderate-magnitude aseismic transients in future seismic swarms.

The finding of the aseismic slip during the pre-M4.6 stage arises the question of whether the largest M4.6 event could be controlled by the precursory slow slip, or either the preslip model or the cascading model is supported. (1) In the preslip model, the preseismic slip weakens the surrounding fault, and the magnitude of an earthquake is controlled primarily by its nucleation process, e.g., the amplitude and area of precursory slip. As observed in the laboratory experiments of frictional sliding (Ohnaka & Kuwahara, 1990; Latour et al., 2013), the nucleation consists of two distinct stages, and both phases are aseismic: (I) an initial quasi-static stage, and (II) the subsequent faster-accelerating stage. We also observe similar acceleration pattern during the pre-M4.6 stage, where the median slip rate increased from 2×10^{-8} m/s (February 26∼March 15) to 6×10^{-8} m/s (March 15∼March 20). There is another possibility that the aseismic slip during the early stage is an independent slow slip event, which is not related to the earthquake nucleation and the triggering of the M4.6 event is incidental. We calculate the cumulative Coulomb stress changes on the hypocenter of five M4+ foreshocks and the M4.6 event based on the modeled slip and the maximum value of the cumulative Coulomb stress change over the seismic rupture regions are 5.3, 6.9, 2.8, 3.9, 0.4, and 4.1 MPa, which is enough to trigger an earthquake (King et al., 1994). (2) In the cascade model, earthquakes occur by neighbor-to-neighbor stress transfer between one foreshock and another without an aseismic slip component, and the eventual mainshock is a random outcome of triggering by ordinary small earthquakes in close enough proximity to the mainshock (Ellsworth & Bulut, 2018). Similarly, we calculate the cumulative Coulomb stress change on five M4+ events and the M4.6 event caused by the earlier earthquakes and the maximum value of the cumulative Coulomb stress changes over the seismic rupture regions is 0.7, 1.1, 3.0, 0.1, 1.1, and 1.5 MPa, which is also higher than 0.01 MPa. It inferred that the M4+ foreshocks and the M4.6 event can also be triggered by the earlier earthquakes. However, this analysis can be affected by many factors, e.g., the precision of earthquake hypocenter, and the stress drop calculation method. For example, an $M_w4.3$ foreshock occurred two hours before the 1992 $M_w6.1$ Joshua Tree earthquake, and Dodge et al. (1996) estimated the Coulomb stress change from the foreshocks at the mainshock hypocenter by assuming a circular source model with a constant stress drop crack model and placing the mainshock hypocenter inside foreshock rupture. They found the Coulomb stress change was almost certainly negative (99.9%) and concluded that the static stress change from the foreshocks was unlikely to initiate the mainshock. In contrast, Mori (1996) calculated a finite slip model for the foreshock where the mainshock hypocenter was outside of the foreshock rupture, and he estimated a quite high stress drop of the foreshock (32∼87 MPa) on the mainshock hypocenter. The opposite conclusions from two different studies imply the resolution limits of foreshock-location-based triggering analysis. To conclude, though limitations in analyzing the Coulomb stress change, the triggering of earthquakes during the initial phase cannot be explained by solely the cascade model, since the large disagreement between the geodetic moment and the seismic moment indicates that seismic slip cannot solely explain the observed surface deformation successfully. As for the largest M4.6 event, we interpret it could have been triggered by earthquake nucleation initialed by aseismic, an independent slow slip event, nearby preceding seismicity, or all of them.

The aseismic slip mainly occurred on the southern subfault during the pre-M4.6 stage, while the most significant seismic slip hit the northern subfault during the co- and post-M4.6 stages. Here we discuss the possible underlying mechanisms of contrasting behaviors on the two subfaults. One potential cause of the precursory aseismic slip on the southern segment is various dilatancy properties along strike. Many authors have studied the shear-induced dilatancy, which could increase the effective normal stress and thus favor fault stability (Segall & Rice, 1995; Segall et al., 2010; Ciardo & Lecampion, 2019). For example, to explain abundant microseismicity and aseismic transients in barrier zones on the Gofar transform fault, Liu et al. (2020) proposed a numerical model where strong dilatancy strengthening effectively stabilizes along-strike seismic rupture propagation and results in rupture barriers where aseismic transients arise. If this is also true for the 2011 Hawthorne seismic swarm, the shear-induced dilatancy would explain the aseismic transients on the southern fault and the seismic rupture on the northern subfault. What's more, the requirement of enhanced fluid-filled porosity for the dilatancy strengthening might be filled for the 2011 Hawthorne sequence. The 2011 Hawthorne sequence is close to the Aurora-Bodie volcano (Lange & Carmichael, 1996), and geothermal fluids have been found in this area (Hinz et al., 2010), so it is possible that excess fluids can be persistently supplied and lead to large fluid-filled porosity and high pore pressure. Therefore, the dilatancy strengthening might be one of the underlying mechanics that govern the partitioning between aseismic and seismic slip during the 2011 Hawthorne earthquake swarm.

In addition, the fault geometrical complexity could favor the lateral variation of slip and aseismic slip. Firstly, Romanet et al. (2018) proposed that two overlapping faults can naturally result in a complex seismic cycle without introducing complex frictional heterogeneities on the fault. They found, for two mildly rate-weakening faults with a small distance between the faults, a complex behavior with a mixture of slow and rapid slip can be observed. This finding is consistent with the mixture of slow and fast slip close to the connecting region of two subfaults during the 2011 Hawthorne swarm (triangular subfault in Figure 8). Secondly, Cattania and Segall (2021) highlights the effect of long-wavelength fault roughness on a range of fault behaviors, foreshocks, and precursory slow slip, during the preparation stage of an energetic event. Their numerical simulation suggested the preparation stage is characterized by feedback between creep and foreshocks: episodic seismic ruptures break neighboring asperity groups and favor the creep acceleration, which loads other asperities leading to further foreshocks consecutively. The coexistence of foreshocks and precursory slow slip, as well as their migration toward the hypocenter of the energetic event in Cattania and Segall (2021), also matched our observation during the pre-4.6 stage (Figure 8). Therefore, we think fault geometrical complexity might contribute to the precursory slow slip during the 2011 Hawthorne earthquake swarm.

6 Conclusion

This study has developed a new methodology for retrieving time-dependent fault distributions, by incorporating a physics-based crack model. We first introduce two propagation patterns of fault ruptures and then propose a method to solve the complex slip distribution with multiple physics-based crack models. Finally, the proposed methodology is demonstrated by simulated experiments and one real seismic swarm case. The advantages of the proposed method are as follows.

(1) To describe a compact slip distribution, a laboratory-derived crack model is used in our inversion method, significantly reducing the number of parameters to solve, independently of the level of fault discretization. Though the degree of freedom is less than in the previous methods, some complexity in the slip pattern can be incorporated by adding multiple partially or totally overlapping ruptures.

(2) The robustness of our method has been demonstrated by simulated cases with various slip patterns and published slip distribution datasets, SRCMOD.

(3) Our proposed method is applied to derive a time-dependent fault slip distribution model for the 2011 Hawthorne seismic swarm (Nevada, USA). The results show that aseismic slip on a southern subfault dominates fault behavior during the pre-M4.6 stage; then during the most energetic stage, the largest event occurred on a northern subfault. Our results are consistent with an overlapping fault slip migration during the pre-M4.6 stage along the southern fault, followed by larger triggered coseismic ruptures of fault patches along the northern fault. Our model favors the identification of small-scale compact slip distribution, and allows us to estimate the peak and average value of fault slip rates. These are consistent with reported values for slow slip events and other continental swarms.

The new inversion method presented is complementary to the existing methodology for retrieving fault-slip distributions. We hope it becomes a useful toolbox to improve the identification of similar precursory slow slip during other long-lasting earthquake sequences (swarms), and help understand the driving mechanisms of earthquakes.

Acknowledgments

This research was supported by the Natural Environmental Research Council (NERC) through the Centre for the Observation and Modeling of Earthquakes, Volcanoes and Tectonics (UK) (GA/13/M/031) and the LiCS large grant (NE/K011006/1). This research was also supported by a Chinese Scholarship Council-University of Liverpool joint scholarship awarded to YJ (201706450071). PJG acknowledged the support of the Spanish Ministerio de Ciencia e Innovación research project, grant agreement number PID2019-104571RA-I00 (COMPACT) and the Beca Leonardo a Investigadores y Creadores Culturales 2020 from the Fundación BBVA. RADARSAT-2 images were acquired under SOAR-E project 28209 from the Canadian Space Agency, and ENVISAT images from ESA CAT1 project 6745. RADARSAT-2 and ENVISAT interferograms in the paper can be downloaded from `https://doi.org/10.5281/zenodo.5043161`. The finite-fault source model SRCMOD is retrieved from `http://equake-rc.info/srcmod/`. The geodetic inversion software slipBERI is retrieved from `https://github.com/ruthamey/slipBERI` and WG-BIS package from `https://doi.org/10.5281/zenodo.3727158`. The CRUST 1.0 model is retrieved from `https://igppweb.ucsd.edu/~gabi/crust1.html`. The manuscript was edited by Guido Jones, currently funded by the Cabildo de Tenerife, under the TFinnova Programme supported by MEDI and FDCAN funds. Thanks go to Mehdi Nikkhoo for providing the triangular dislocation functions for displacement gradient tensor. The authors are also grateful to Tim Wright, Dan Faulkner, and Louisa Brotherson for insightful discussions of different aspects of this study, as well as to editor Rachel Abercrombie, associate editor, Eric Lindsey, and another anonymous reviewer for their helpful and constructive reviews, which greatly improved this manuscript.

References

Ainscoe, E. A., Elliott, J. R., Copley, A., Craig, T. J., Li, T., Parsons, B. E., & Walker, R. T. (2017). Blind Thrusting, Surface Folding, and the Development of Geological Structure in the Mw 6.3 2015 Pishan (China) Earthquake. *Journal of Geophysical Research: Solid Earth*, *122*(11), 9359–9382. doi: 10.1002/2017JB014268

Amey, R. M. J., Hooper, A., & Walters, R. J. (2018). A Bayesian Method for Incorporating Self-Similarity Into Earthquake Slip Inversions. *Journal of Geophysical Research: Solid Earth*, *123*(7), 6052–6071. doi: 10.1029/2017JB015316

Argus, D. F., & Gordon, R. G. (1991). Current Sierra Nevada-North America motion from very long baseline interferometry: Implications for the kinematics of the western United States. *Geology*, *19*(11), 1085–1088.

Aster, R. C., Borchers, B., & Thurber, C. H. (2019). Chapter three - rank deficiency and ill-conditioning. In R. C. Aster, B. Borchers, & C. H. Thurber (Eds.), *Parameter estimation and inverse problems* (Third Edition ed., p. 55-91). Elsevier. doi: 10.1016/B978-0-12-804651-7.00008-0

Bagnardi, M., & Hooper, A. (2018). Inversion of Surface Deformation Data for Rapid Estimates of Source Parameters and Uncertainties: A Bayesian Approach. *Geochemistry, Geophysics, Geosystems*, *19*(7), 2194–2211. doi: 10.1029/2018GC007585

Barnhart, W. D., Benz, H. M., Hayes, G. P., Rubinstein, J. L., & Bergman, E. (2014). Seismological and geodetic constraints on the 2011 Mw5.3 Trinidad, Colorado earthquake and induced deformation in the Raton Basin. *Journal of Geophysical Research: Solid Earth*, *119*(10), 7923–7933. doi: 10.1002/2014JB011227

Barnhart, W. D., & Lohman, R. B. (2010). Automated fault model discretization for inversions for coseismic slip distributions. *Journal of Geophysical Research: Solid Earth*, *115*(B10). doi: 10.1029/2010JB007545

Barnhart, W. D., Murray, J. R., Briggs, R. W., Gomez, F., Miles, C. P., Svarc, J., ... Stressler, B. J. (2016). Coseismic slip and early afterslip of the 2015 Illapel, Chile, earthquake: Implications for frictional heterogeneity and coastal uplift. *Journal of Geophysical Research: Solid Earth*, *121*(8), 6172–6191. doi: 10.1002/2016JB013124

Bedford, J., Moreno, M., Baez, J. C., Lange, D., Tilmann, F., Rosenau, M., ... Vigny, C. (2013). A high-resolution, time-variable afterslip model for the 2010 Maule Mw=8.8, Chile megathrust earthquake. *Earth and Planetary Science Letters*, *383*, 26–36. doi: 10.1016/j.epsl.2013.09.020

Bennett, R. A., Reilinger, R. E., Rodi, W., Yingping Li, Toksoz, M. N., & Hudnut, K. (1995). Coseismic fault slip associated with the 1992 M w 6.1 Joshua Tree, California, earthquake: Implications for the Joshua Tree-Landers earthquake sequence. *Journal of Geophysical Research: Solid Earth*, *100*(B4), 6443–6461. doi: 10.1029/94JB02944

Bhattacharya, P., & Viesca, R. C. (2019). Fluid-induced aseismic fault slip outpaces pore-fluid migration. *Science*, *364*(6439), 464–468. doi: 10.1126/science.aaw7354

Biggs, J., Bergman, E., Emmerson, B., Funning, G. J., Jackson, J., Parsons, B., & Wright, T. J. (2006). Fault identification for buried strike-slip earthquakes using InSAR: The 1994 and 2004 Al Hoceima, Morocco earthquakes. *Geophysical Journal International*, *166*(3), 1347–1362. doi: 10.1111/j.1365-246X.2006.03071.x

Bletery, Q., & Nocquet, J. M. (2020). Slip bursts during coalescence of slow slip events in Cascadia. *Nature Communications*, *11*(1), 1–6. doi: 10.1038/s41467-020-15494-4

Bormann, J. M., Hammond, W. C., Kreemer, C., & Blewitt, G. (2016). Accommodation of missing shear strain in the Central Walker Lane, western North America: Constraints from dense GPS measurements. *Earth and Planetary Science Letters*, *440*, 169–177. doi: 10.1016/j.epsl.2016.01.015

Brune, J. N. (1970). Tectonic stress and the spectra of seismic shear waves from earthquakes. *Journal of Geophysical Research*, *75*(26), 4997–5009. doi: 10.1029/JB075I026P04997

Bürgmann, R., Ergintav, S., Segall, P., Hearn, E., McClusky, S., Reilinger, R., ... Zschau, J. (2002). Time-Dependent Distributed Afterslip on and Deep below the İzmit Earthquake Rupture. *Bulletin of the Seismological Society of America*, *92*, 126–137. doi: 10.1785/0120000833

Caballero, E., Chounet, A., Duputel, Z., Jara, J., Twardzik, C., & Jolivet, R. (2021). Seismic and Aseismic Fault Slip During the Initiation Phase of the

2017 Mw = 6.9 Valparaíso Earthquake. *Geophysical Research Letters*, *48*(6), e2020GL091916. doi: 10.1029/2020GL091916

Cappa, F., Scuderi, M. M., Collettini, C., Guglielmi, Y., & Avouac, J. P. (2019). Stabilization of fault slip by fluid injection in the laboratory and in situ. *Science Advances*, *5*(3), eaau4065. doi: 10.1126/sciadv.aau4065

Cattania, C., & Segall, P. (2021). Precursory slow slip and foreshocks on rough faults. *Journal of Geophysical Research: Solid Earth*, e2020JB020430. doi: 10.1029/2020JB020430

Champenois, J., Baize, S., Vallee, M., Jomard, H., Alvarado, A., Espin, P., … Audin, L. (2017). Evidences of Surface Rupture Associated With a Low-Magnitude (Mw 5.0) Shallow Earthquake in the Ecuadorian Andes. *Journal of Geophysical Research: Solid Earth*, *122*(10), 8446–8458. doi: 10.1002/2017JB013928

Cheloni, D., D'Agostino, N., Selvaggi, G., Avallone, A., Fornaro, G., Giuliani, R., … Tizzani, P. (2017). Aseismic transient during the 2010-2014 seismic swarm: Evidence for longer recurrence of M≥6.5 earthquakes in the Pollino gap (Southern Italy)? *Scientific Reports*, *7*(1), 1–10. doi: 10.1038/s41598-017-00649-z

Ciardo, F., & Lecampion, B. (2019). Effect of Dilatancy on the Transition From Aseismic to Seismic Slip Due to Fluid Injection in a Fault. *Journal of Geophysical Research: Solid Earth*, *124*(4), 3724–3743. doi: 10.1029/2018JB016636

De Barros, L., Cappa, F., Deschamps, A., & Dublanchet, P. (2020). Imbricated Aseismic Slip and Fluid Diffusion Drive a Seismic Swarm in the Corinth Gulf, Greece. *Geophysical Research Letters*, *47*(9). doi: 10.1029/2020GL087142

Delorey, A. A., van der Elst, N. J., & Johnson, P. A. (2017). Tidal triggering of earthquakes suggests poroelastic behavior on the San Andreas Fault. *Earth and Planetary Science Letters*, *460*, 164–170. doi: 10.1016/j.epsl.2016.12.014

Di Carli, S., François-Holden, C., Peyrat, S., & Madariaga, R. (2010). Dynamic inversion of the 2000 Tottori earthquake based on elliptical subfault approximations. *Journal of Geophysical Research*, *115*(B12), B12328. doi: 10.1029/2009JB006358

Dodge, D. A., Beroza, G. C., & Ellsworth, W. L. (1996). Detailed observations of California foreshock sequences: Implications for the earthquake initiation process. *Journal of Geophysical Research: Solid Earth*, *101*(B10), 22371–22392. doi: 10.1029/96JB02269

Du, Y., Aydin, A., & Segall, P. (1992). Comparison of various inversion techniques as applied to the determination of a geophysical deformation model for the 1983 Borah Peak earthquake. *Bulletin of the Seismological Society of America*, *82*(4), 1840–1866.

Elliott, J. R., Walters, R. J., England, P. C., Jackson, J. A., Li, Z., & Parsons, B. (2010). Extension on the Tibetan plateau: recent normal faulting measured by InSAR and body wave seismology. *Geophysical Journal International*, *183*(2), 503–535. doi: 10.1111/j.1365-246X.2010.04754.x

Ellsworth, W. L., & Bulut, F. (2018, jun). Nucleation of the 1999 Izmit earthquake by a triggered cascade of foreshocks. *Nature Geoscience*, *11*(7), 531-535. doi: 10.1038/s41561-018-0145-1

Engwirda, D. (2014). *Locally optimal Delaunay-refinement and optimisation-based mesh generation* (Doctoral dissertation, University of Sydney). Retrieved from `http://hdl.handle.net/2123/13148`

Faulds, J., & Henry, C. (2008). Tectonic influences on the spatial and temporal evolution of the Walker Lane: An incipient transform fault along the evolving Pacific - North American plate boundary. *Arizona Geological Society Digest*, *22*, 437–470.

Floyd, M. A., Walters, R. J., Elliott, J. R., Funning, G. J., Svarc, J. L., Murray, J. R., ... Wright, T. J. (2016, jul). Spatial variations in fault friction related to lithology from rupture and afterslip of the 2014 South Napa, California, earthquake. *Geophysical Research Letters*, *43*(13), 6808–6816. Retrieved from `https://onlinelibrary.wiley.com/doi/full/10.1002/2016GL069428https://onlinelibrary.wiley.com/doi/abs/10.1002/2016GL069428https://agupubs.onlinelibrary.wiley.com/doi/10.1002/2016GL069428` doi: 10.1002/2016GL069428

Fukahata, Y., & Wright, T. J. (2008). A non-linear geodetic data inversion using ABIC for slip distribution on a fault with an unknown dip angle. *Geophysical Journal International*, *173*(2), 353–364. doi: 10.1111/j.1365-246X.2007.03713.x

Fukuda, J. (2018). Variability of the Space-Time Evolution of Slow Slip Events Off the Boso Peninsula, Central Japan, From 1996 to 2014. *Journal of Geophysical Research: Solid Earth*, *123*(1), 732–760. doi: 10.1002/2017JB014709

Fukuda, J., & Johnson, K. M. (2008). A fully Bayesian inversion for spatial distribution of fault slip with objective smoothing. *Bulletin of the Seismological Society of America*, *98*(3), 1128–1146. doi: 10.1785/0120070194

Fukuda, J., & Johnson, K. M. (2010). Mixed linear-non-linear inversion of crustal deformation data: Bayesian inference of model, weighting and regularization parameters. *Geophysical Journal International*, *181*(3), 1441–1458. doi: 10.1111/j.1365-246X.2010.04564.x

Gavish, M., & Donoho, D. L. (2014). The optimal hard threshold for singular values is $4/\sqrt{3}$. *IEEE Transactions on Information Theory*, *60*(8), 5040–5053. doi: 10.1109/TIT.2014.2323359

Gomberg, J. (2018). Unsettled earthquake nucleation. *Nature Geoscience*, *11*(7), 463–464. doi: 10.1038/s41561-018-0149-x

Gomberg, J., & Johnson, P. (2005). Dynamic triggering of earthquakes. *Nature*, *437*(7060), 830. doi: 10.1038/437830a

González, P. J., Samsonov, S. V., Pepe, S., Tiampo, K. F., Tizzani, P., Casu, F., ... Sansosti, E. (2013). Magma storage and migration associated with the 2011-2012 El Hierro eruption: Implications for crustal magmatic systems at oceanic island volcanoes. *Journal of Geophysical Research: Solid Earth*, *118*(8), 4361–4377. doi: 10.1002/jgrb.50289

Grandin, R., Socquet, A., Doin, M.-P., Jacques, E., de Chabalier, J.-B., & King, G. C. P. (2010). Transient rift opening in response to multiple dike injections in the Manda Hararo rift (Afar, Ethiopia) imaged by time-dependent elastic inversion of interferometric synthetic aperture radar data. *Journal of Geophysical Research*, *115*(B9), B09403. doi: 10.1029/2009JB006883

Gualandi, A., Nichele, C., Serpelloni, E., Chiaraluce, L., Anderlini, L., Latorre, D., ... Avouac, J.-P. (2017). Aseismic deformation associated with an earthquake swarm in the northern Apennines (Italy). *Geophysical Research Letters*, *44*(15), 7706–7714. doi: 10.1002/2017GL073687

Guglielmi, Y., Cappa, F., Avouac, J. P., Henry, P., & Elsworth, D. (2015). Seismicity triggered by fluid injection-induced aseismic slip. *Science*, *348*(6240), 1224–1226. doi: 10.1126/science.aab0476

Hamling, I. J., Hreinsdóttir, S., Clark, K., Elliott, J., Liang, C., Fielding, E., ... Stirling, M. (2017). Complex multifault rupture during the 2016 Mw 7.8 Kaikōura earthquake, New Zealand. *Science*, *356*(6334). doi: 10.1126/science.aam7194

Hammond, W. C., & Thatcher, W. (2007). Crustal deformation across the Sierra Nevada, northern Walker Lane, Basin and Range transition, western United States measured with GPS, 2000–2004. *Journal of Geophysical Research: Solid Earth*, *112*(B5), 5411. doi: 10.1029/2006JB004625

Harris, R. A., & Segall, P. (1987). Detection of a locked zone at depth on the Parkfield, California, segment of the San Andreas Fault. *Journal of Geophysical Research*, *92*(B8), 7945. doi: 10.1029/JB092iB08p07945

Hatch, R. L. (2020). *Characterization of Recent Earthquake Sequences and Swarms Within the Walker Lane Tectonic Region* (Doctoral dissertation, University of Nevada, Reno). Retrieved from `http://hdl.handle.net/11714/7569`

Hatch, R. L., Abercrombie, R. E., Ruhl, C. J., & Smith, K. D. (2018). Earthquake Interaction, Fault Structure, and Source Properties of a Small Sequence in 2017 near Truckee, CaliforniaEarthquake Interaction, Fault Structure, and Source Properties of a Small Sequence in 2017 near Truckee. *Bulletin of the Seismological Society of America*, *108*(5A), 2580–2593. doi: 10.1785/0120180089

Hatch, R. L., Abercrombie, R. E., Ruhl, C. J., & Smith, K. D. (2020). Evidence of Aseismic and Fluid-Driven Processes in a Small Complex Seismic Swarm Near Virginia City, Nevada. *Geophysical Research Letters*, *47*(4), e2019GL085477. doi: 10.1029/2019GL085477

Hicks, S. P., Okuwaki, R., Steinberg, A., Rychert, C. A., Harmon, N., Abercrombie, R. E., ... Sudhaus, H. (2020). Back-propagating supershear rupture in the 2016 Mw 7.1 Romanche transform fault earthquake. *Nature Geoscience*, *13*(9), 647–653. doi: 10.1038/s41561-020-0619-9

Hinz, N., Faulds, J., Moeck, I., Bell, J. W., & Oldow, J. S. (2010). Structural controls of three blind geothermal resources at the hawthorne ammunition depot, West-Central Nevada. *Transactions - Geothermal Resources Council*, *34*, 720–725.

Hirose, H., & Obara, K. (2010). Recurrence behavior of short-term slow slip and correlated nonvolcanic tremor episodes in western Shikoku, southwest Japan. *Journal of Geophysical Research: Solid Earth*, *115*(B6), 0–21. doi: 10.1029/2008JB006050

Houston, H., Delbridge, B. G., Wech, A. G., & Creager, K. C. (2011). Rapid tremor reversals in Cascadia generated by a weakened plate interface. *Nature Geoscience*, *4*(6), 404–409. doi: 10.1038/ngeo1157

Hussain, E., Hooper, A., Wright, T. J., Walters, R. J., & Bekaert, D. P. (2016). Interseismic strain accumulation across the central North Anatolian Fault from iteratively unwrapped InSAR measurements. *Journal of Geophysical Research: Solid Earth*, *121*(12), 9000–9019. doi: 10.1002/2016JB013108

Ichinose, G. A., Anderson, J. G., Smith, K. D., & Zeng, Y. (2003). Source Parameters of Eastern California and Western Nevada Earthquakes from Regional Moment Tensor Inversion. *Bulletin of the Seismological Society of America*, *93*(1), 61–84. doi: 10.1785/0120020063

Ingleby, T., Wright, T. J., Hooper, A., Craig, T. J., & Elliott, J. R. (2020, feb). Constraints on the Geometry and Frictional Properties of the Main Himalayan Thrust Using Coseismic, Postseismic, and Interseismic Deformation in Nepal. *Journal of Geophysical Research: Solid Earth*, *125*(2), e2019JB019201. Retrieved from `https://onlinelibrary.wiley.com/doi/full/10.1029/2019JB019201https://onlinelibrary.wiley.com/doi/abs/10.1029/2019JB019201https://agupubs.onlinelibrary.wiley.com/doi/10.1029/2019JB019201` doi: 10.1029/2019JB019201

Jiang, Y., & González, P. J. (2020). Bayesian Inversion of Wrapped Satellite Interferometric Phase to Estimate Fault and Volcano Surface Ground Deformation Models. *Journal of Geophysical Research: Solid Earth*, *125*(5). doi: 10.1029/2019JB018313

Jiang, Y., & González, P. J. (2021). High-resolution spatio-temporal fault slip using InSAR observations: insights on seismic and aseismic slip during a shallow crust earthquake swarm. In *EGU General Assembly Conference Abstracts.* doi: 10.5194/egusphere-egu21-6280

Jiang, Y., González, P. J., & Bürgmann, R. (2021). Subduction earthquakes controlled by incoming plate geometry: The 2020 M>7.5 Shumagin, Alaska, earthquake doublet. *EarthArXiv*. doi: 10.31223/X5H91J

Johanson, I. A., & Bürgmann, R. (2005). Creep and quakes on the northern transition zone of the San Andreas fault from GPS and InSAR data. *Geophysical Research Letters*, *32*(14), 1–5. doi: 10.1029/2005GL023150

Johnson, K. M., Fukuda, J., & Segall, P. (2012). Challenging the rate-state asperity model: Afterslip following the 2011 M9 Tohoku-oki, Japan, earthquake. *Geophysical Research Letters*, *39*(20), 2012GL052901. doi: 10.1029/2012GL052901

Jolivet, R., Lasserre, C., Doin, M. P., Guillaso, S., Peltzer, G., Dailu, R., ... Xu, X. (2012). Shallow creep on the Haiyuan Fault (Gansu, China) revealed by SAR Interferometry. *Journal of Geophysical Research: Solid Earth*, *117*(B6), 6401. doi: 10.1029/2011JB008732

Kampes, B., Hanssen, R., & Perski, Z. (2003). Radar interferometry with public domain tools. *Proc. of FRINGE 2003 Workshop*.

Kaneko, Y., & Shearer, P. M. (2014). Seismic source spectra and estimated stress drop derived from cohesive-zone models of circular subshear rupture. *Geophysical Journal International*, *197*(2), 1002–1015. doi: 10.1093/gji/ggu030

Ke, C.-Y., McLaskey, G. C., & Kammer, D. S. (2020). The Earthquake Arrest Zone. *Geophysical Journal International*. doi: 10.1093/gji/ggaa386

Khoshmanesh, M., Shirzaei, M., & Nadeau, R. M. (2015). Time-dependent model of aseismic slip on the central San Andreas Fault from InSAR time series and repeating earthquakes. *Journal of Geophysical Research: Solid Earth*, *120*(9), 6658–6679. doi: 10.1002/2015JB012039

King, G. C. P., Stein, R. S., & Lin, J. (1994, jun). Static stress changes and the triggering of earthquakes. *Bulletin of the Seismological Society of America*, *84*(3), 935-953.

Klein, E., Duputel, Z., Zigone, D., Vigny, C., Boy, J.-P., Doubre, C., & Meneses, G. (2018). Deep transient slow slip detected by survey gps in the region of atacama, chile. *Geophysical Research Letters*, *45*(22), 12,263-12,273. doi: 10.1029/2018GL080613

Kreemer, C., Blewitt, G., & Hammond, W. C. (2009). Geodetic constraints on contemporary deformation in the northern Walker Lane: 2. Velocity and strain rate tensor analysis. In *Late Cenozoic Structure and Evolution of the Great Basin-Sierra Nevada Transition.* Geological Society of America. doi:

10.1130/2009.2447(02)

Kreemer, C., Blewitt, G., & Klein, E. C. (2014). A geodetic plate motion and Global Strain Rate Model. *Geochemistry, Geophysics, Geosystems*, *15*(10), 3849–3889. doi: 10.1002/2014GC005407

Kyriakopoulos, C., Chini, M., Bignami, C., Stramondo, S., Ganas, A., Kolligri, M., & Moshou, A. (2013). Monthly migration of a tectonic seismic swarm detected by DInSAR: Southwest Peloponnese, Greece. *Geophysical Journal International*, *194*(3), 1302–1309. doi: 10.1093/gji/ggt196

Lambert, V., Lapusta, N., & Perry, S. (2021). Propagation of large earthquakes as self-healing pulses or mild cracks. *Nature*, *591*(7849), 252–258. doi: 10.1038/s41586-021-03248-1

Lange, R. A., & Carmichael, I. S. E. (1996). The Aurora volcanic field, California-Nevada: oxygen fugacity constraints on the development of andesitic magma. *Contributions to Mineralogy and Petrology*, *125*(2), 167–185. doi: 10.1007/s004100050214

Latour, S., Schubnel, A., Nielsen, S., Madariaga, R., & Vinciguerra, S. (2013, oct). Characterization of nucleation during laboratory earthquakes. *Geophysical Research Letters*, *40*(19), 5064-5069. doi: 10.1002/GRL.50974

Liu, Y., McGuire, J. J., & Behn, M. D. (2020). Aseismic transient slip on the Gofar transform fault, East Pacific Rise. *Proceedings of the National Academy of Sciences of the United States of America*, *117*(19), 10188–10194. doi: 10.1073/pnas.1913625117

Lohman, R. B., & McGuire, J. J. (2007). Earthquake swarms driven by aseismic creep in the Salton Trough, California. *Journal of Geophysical Research: Solid Earth*, *112*(4). doi: 10.1029/2006JB004596

Luo, Y., & Liu, Z. (2019). Rate-and-State Model Casts New Insight into Episodic Tremor and Slow-slip Variability in Cascadia. *Geophysical Research Letters*, *46*(12), 6352–6362. doi: 10.1029/2019GL082694

Madariaga, R. (1976). Dynamics of an expanding circular fault. *Bulletin of the Seismological Society of America*, *66*(3), 639–666.

Mai, P. M., & Beroza, G. C. (2002). A spatial random field model to characterize complexity in earthquake slip. *Journal of Geophysical Research: Solid Earth*, *107*(B11), ESE 10–1–ESE 10–21. doi: 10.1029/2001jb000588

Mai, P. M., & Thingbaijam, K. K. (2014). SRCMOD: An online database of finite-fault rupture models. *Seismological Research Letters*, *85*(6), 1348–1357. doi: 10.1785/0220140077

Marone, C., & Richardson, E. (2006). Do earthquakes rupture piece by piece or all together? *Science*, *313*(5794), 1748-1749. doi: 10.1126/science.1131296

Matthews, M. V., & Segall, P. (1993). Estimation of depth-dependent fault slip from measured surface deformation with application to the 1906 San Francisco earthquake. *Journal of Geophysical Research*, *98*(B7), 12153–12163. doi: 10.1029/93jb00440

Mesimeri, M., & Karakostas, V. (2018). Repeating earthquakes in western Corinth Gulf (Greece): Implications for aseismic slip near locked faults. *Geophysical Journal International*, *215*(1), 659–676. doi: 10.1093/gji/ggy301

Michel, S., Gualandi, A., & Avouac, J. P. (2019). Similar scaling laws for earthquakes and Cascadia slow-slip events. *Nature*, *574*(7779), 522–526. doi: 10.1038/s41586-019-1673-6

Minson, S. E., Simons, M., & Beck, J. L. (2013). Bayesian inversion for finite fault earthquake source models I—theory and algorithm. *Geophysical Journal International*, *194*(3), 1701–1726. doi: 10.1093/gji/ggt180

Mori, J. (1996). Rupture directivity and slip distribution of the M 4.3 foreshock to the 1992 Joshua Tree earthquake, Southern California. *Bulletin of the Seismological Society of America*, *86*(3), 805–810. doi: 10.1785/BSSA0860030805

Nadeau, R. M., & McEvilly, T. V. (1999). Fault slip rates at depth from recurrence intervals of repeating microearthquakes. *Science*, *285*(5428), 718–721. doi: 10.1126/science.285.5428.718

Nissen, E., Ghorashi, M., Jackson, J., Parsons, B., & Talebian, M. (2007). The 2005 Qeshm Island earthquake (Iran) - A link between buried reverse faulting and surface folding in the Zagros Simply Folded Belt? *Geophysical Journal International*, *171*(1), 326–338. doi: 10.1111/j.1365-246X.2007.03514.x

Ohnaka, M., & Kuwahara, Y. (1990). Characteristic features of local breakdown near a crack-tip in the transition zone from nucleation to unstable rupture during stick-slip shear failure. *Tectonophysics*, *175*(1), 197-220. doi: https://doi.org/10.1016/0040-1951(90)90138-X

Ozawa, S., Yarai, H., & Kobayashi, T. (2019). Recovery of the recurrence interval of

Boso slow slip events in Japan. *Earth, Planets and Space*, *71*(1), 1–8. doi: 10.1186/s40623-019-1058-y

Parotidis, M., Rothert, E., & Shapiro, S. A. (2003). Pore-pressure diffusion: A possible triggering mechanism for the earthquake swarms 2000 in Vogtland/NW-Bohemia, central Europe. *Geophysical Research Letters*, *30*(20), 2003GL018110. doi: 10.1029/2003GL018110

Passarelli, L., Rivalta, E., Jónsson, S., Hensch, M., Metzger, S., Jakobsdóttir, S. S., … Dahm, T. (2018). Scaling and spatial complementarity of tectonic earthquake swarms. *Earth and Planetary Science Letters*, *482*, 62–70. doi: 10.1016/j.epsl.2017.10.052

Pritchard, M. E., & Simons, M. (2006). An aseismic slip pulse in northern Chile and along-strike variations in seismogenic behavior. *Journal of Geophysical Research: Solid Earth*, *111*(8). doi: 10.1029/2006JB004258

Radiguet, M., Cotton, F., Vergnolle, M., Campillo, M., Valette, B., Kostoglodov, V., & Cotte, N. (2011). Spatial and temporal evolution of a long term slow slip event: the 2006 Guerrero Slow Slip Event. *Geophysical Journal International*, *184*(2), 816–828. doi: 10.1111/j.1365-246X.2010.04866.x

Radiguet, M., Perfettini, H., Cotte, N., Gualandi, A., Valette, B., Kostoglodov, V., … Campillo, M. (2016). Triggering of the 2014 Mw7.3 Papanoa earthquake by a slow slip event in Guerrero, Mexico. *Nature Geoscience 2016 9:11*, *9*(11), 829–833. doi: 10.1038/ngeo2817

Ragon, T., Sladen, A., & Simons, M. (2018). Accounting for uncertain fault geometry in earthquake source inversions – I: theory and simplified application. *Geophysical Journal International*, *214*(2), 1174–1190. doi: 10.1093/gji/ggy187

Romanet, P., Bhat, H. S., Jolivet, R., & Madariaga, R. (2018). Fast and Slow Slip Events Emerge Due to Fault Geometrical Complexity. *Geophysical Research Letters*, *45*(10), 4809–4819. doi: 10.1029/2018GL077579

Rousset, B., Fu, Y., Bartlow, N., & Bürgmann, R. (2019). Weeks-Long and Years-Long Slow Slip and Tectonic Tremor Episodes on the South Central Alaska Megathrust. *Journal of Geophysical Research: Solid Earth*, *124*(12), 13392–13403. doi: 10.1029/2019JB018724

Ruhl, C. J., Abercrombie, R. E., & Smith, K. D. (2017). Spatiotemporal Variation of Stress Drop During the 2008 Mogul, Nevada, Earthquake Swarm. *Jour-*

nal of Geophysical Research: Solid Earth, *122*(10), 8163–8180. doi: 10.1002/2017JB014601

Ruhl, C. J., Abercrombie, R. E., Smith, K. D., & Zaliapin, I. (2016). Complex spatiotemporal evolution of the 2008 Mw 4.9 Mogul earthquake swarm (Reno, Nevada): Interplay of fluid and faulting. *Journal of Geophysical Research: Solid Earth*, *121*(11), 8196–8216. doi: 10.1002/2016JB013399

Ruhl, C. J., Morton, E. A., Bormann, J. M., Hatch-Ibarra, R., Ichinose, G., & Smith, K. D. (2021). Complex Fault Geometry of the 2020 Mww 6.5 Monte Cristo Range, Nevada, Earthquake Sequence. *Seismological Research Letters*, *92*(3), 1876–1890. doi: 10.1785/0220200345

Salman, R., Hill, E. M., Feng, L., Lindsey, E. O., Mele Veedu, D., Barbot, S., ... Natawidjaja, D. H. (2017). Piecemeal Rupture of the Mentawai Patch, Sumatra: The 2008 Mw 7.2 North Pagai Earthquake Sequence. *Journal of Geophysical Research: Solid Earth*, *122*(11), 9404–9419. doi: 10.1002/2017JB014341

Samsonov, S., & D'Oreye, N. (2012). Multidimensional time-series analysis of ground deformation from multiple InSAR data sets applied to Virunga Volcanic Province. *Geophysical Journal International*, *191*(3), 1095–1108. doi: 10.1111/j.1365-246X.2012.05669.x

Schmidt, D. A., Bürgmann, R., Nadeau, R. M., & D'Alessio, M. (2005). Distribution of aseismic slip rate on the Hayward fault inferred from seismic and geodetic data. *Journal of Geophysical Research: Solid Earth*, *110*(B8), 1–15. doi: 10.1029/2004JB003397

Scott, C., Bunds, M., Shirzaei, M., & Toke, N. (2020). Creep Along the Central San Andreas Fault From Surface Fractures, Topographic Differencing, and InSAR. *Journal of Geophysical Research: Solid Earth*, *125*(10), e2020JB019762. doi: 10.1029/2020JB019762

Segall, P., & Rice, J. R. (1995). Dilatancy, compaction, and slip instability of a fluid-infiltrated fault. *Journal of Geophysical Research: Solid Earth*, *100*(B11), 22155–22171. doi: 10.1029/95JB02403

Segall, P., Rubin, A. M., Bradley, A. M., & Rice, J. R. (2010). Dilatant strengthening as a mechanism for slow slip events. *Journal of Geophysical Research*, *115*(B12), B12305. doi: 10.1029/2010JB007449

Shearer, P. M., Prieto, G. A., & Hauksson, E. (2006). Comprehensive analysis of earthquake source spectra in southern California. *Journal of Geophysical Research: Solid Earth*, *111*(B6), 6303. doi: 10.1029/2005JB003979

Shen, Z. K., Sun, J., Zhang, P., Wan, Y., Wang, M., Bürgmann, R., … Wang, Q. (2009). Slip maxima at fault junctions and rupturing of barriers during the 2008 Wenchuan earthquake. *Nature Geoscience*, *2*(10), 718–724. doi: 10.1038/ngeo636

Smith, K., Johnson, C., Davies, J., Agbaje, T., Knezevic Antonijevic, S., & Kent, G. (2011). The 2011 Hawthorne, Nevada, Earthquake Sequence: Shallow Normal Faulting. In *AGU Fall Meeting* (pp. S53B–2284).

Song, X., Jiang, Y., Shan, X., Gong, W., & Qu, C. (2019). A Fine Velocity and Strain Rate Field of Present-Day Crustal Motion of the Northeastern Tibetan Plateau Inverted Jointly by InSAR and GPS. *Remote Sensing 2019, Vol. 11, Page 435*, *11*(4), 435. doi: 10.3390/RS11040435

Stein, S., & Gordon, R. G. (1984). Statistical tests of additional plate boundaries from plate motion inversions. *Earth and Planetary Science Letters*, *69*(2), 401–412. doi: 10.1016/0012-821X(84)90198-5

Sun, J., Johnson, K. M., Cao, Z., Shen, Z., Bürgmann, R., & Xu, X. (2011). Mechanical constraints on inversion of coseismic geodetic data for fault slip and geometry: Example from InSAR observation of the 6 October 2008 Mw 6.3 Dangxiong-Yangyi (Tibet) earthquake. *Journal of Geophysical Research*, *116*(B1), B01406. doi: 10.1029/2010JB007849

Takenaka, H., & Fujii, Y. (2008). A compact representation of spatio-temporal slip distribution on a rupturing fault. *Journal of Seismology*, *12*, 281-293. doi: 10.1007/s10950-007-9087-6

Taymaz, T., Wright, T. J., Yolsal, S., Tan, O., Fielding, E., & Seyitoğlu, G. (2007). Source characteristics of the 6 June 2000 Orta-Çankiri (central Turkey) earthquake: A synthesis of seismological,geological and geodetic (InSAR) observations, and internal deformation of the Anatolian plate. *Geological Society Special Publication*, *291*(1), 259–290. doi: 10.1144/SP291.12

Thomas, M. Y., Avouac, J.-P., Champenois, J., Lee, J.-C., Kuo, L.-C., Thomas, M. Y., … Kuo, L.-C. (2014). Spatiotemporal evolution of seismic and aseismic slip on the Longitudinal Valley Fault, Taiwan. *Journal of Geophysical Research: Solid Earth*, *119*(6), 5114–5139. doi: 10.1002/2013JB010603

Tridon, M., Cayol, V., Froger, J., Augier, A., & Bachèlery, P. (2016). Inversion of coeval shear and normal stress of Piton de la Fournaise flank displacement. *Journal of Geophysical Research: Solid Earth*, *121*(11), 7846–7866. doi: 10.1002/2016JB013330

Tsang, L. L. H., Hill, E. M., Barbot, S., Qiu, Q., Feng, L., Hermawan, I., … Natawidjaja, D. H. (2016). Afterslip following the 2007 Mw 8.4 Bengkulu earthquake in Sumatra loaded the 2010 Mw 7.8 Mentawai tsunami earthquake rupture zone. *Journal of Geophysical Research: Solid Earth*, *121*(12), 9034–9049. doi: 10.1002/2016JB013432

Turner, R. C., Nadeau, R. M., & Bürgmann, R. (2013). Aseismic slip and fault interaction from repeating earthquakes in the Loma Prieta aftershock zone. *Geophysical Research Letters*, *40*(6), 1079–1083. doi: 10.1002/grl.50212

Uchide, T., Shearer, P. M., & Imanishi, K. (2014). Stress drop variations among small earthquakes before the 2011 Tohoku-oki, Japan, earthquake and implications for the main shock. *Journal of Geophysical Research: Solid Earth*, *119*(9), 7164–7174. doi: 10.1002/2014JB010943

Villegas-Lanza, J. C., Nocquet, J. M., Rolandone, F., Vallee, M., Tavera, H., Bondoux, F., … Chlieh, M. (2016). A mixed seismic-aseismic stress release episode in the Andean subduction zone. *Nature Geoscience*, *9*(2), 150–154. doi: 10.1038/ngeo2620

Wallace, L. M. (2020). Slow slip events in new zealand. *Annual Review of Earth and Planetary Sciences*, *48*(1), 175-203. doi: 10.1146/annurev-earth-071719-055104

Wallace, L. M., Beavan, J., Bannister, S., & Williams, C. (2012). Simultaneous long-term and short-term slow slip events at the Hikurangi subduction margin, New Zealand: Implications for processes that control slow slip event occurrence, duration, and migration. *Journal of Geophysical Research B: Solid Earth*, *117*(11). doi: 10.1029/2012JB009489

Walters, R. J., Elliott, J. R., D'Agostino, N., England, P. C., Hunstad, I., Jackson, J. A., … Roberts Edinburgh, G. (2009). The 2009 L'Aquila earthquake (central Italy): A source mechanism and implications for seismic hazard. *Geophysical Research Letters*, *36*(17). doi: 10.1029/2009GL039337

Wech, A. G., Creager, K. C., & Melbourne, T. I. (2009). Seismic and geodetic constraints on Cascadia slow slip. *Journal of Geophysical Research: Solid Earth*, *114*(10). doi: 10.1029/2008JB006090

Werner, C. (2000). GAMMA SAR and interferometric processing software. *Proceedings of ERS-Envisat Symposium ; 16-20 October, Gothenburg, Sweden, 2000*.

Wesnousky, S. (2005). Active faulting in the walker lane. *Tectonics*, *24*(3). doi: 10.1029/2004TC001645

Wesnousky, S. (2021). *The Walker Lane: A Potential Target for SCEC Studies? — Southern California Earthquake Center.* Retrieved 2022-01-07, from `https://www.scec.org/article/731`

Wicks, C., Thelen, W., Weaver, C., Gomberg, J., Rohay, A., & Bodin, P. (2011). InSAR observations of aseismic slip associated with an earthquake swarm in the Columbia River flood basalts. *Journal of Geophysical Research*, *116*(B12), B12304. doi: 10.1029/2011JB008433

Xu, W., Bürgmann, R., & Li, Z. (2016). An improved geodetic source model for the 1999 Mw 6.3 Chamoli earthquake, India. *Geophysical Journal International*, *205*(1), 236–242. doi: 10.1093/gji/ggw016

Yamashita, Y., Yakiwara, H., Asano, Y., Shimizu, H., Uchida, K., Hirano, S., ... Obara, K. (2015). Migrating tremor off southern Kyushu as evidence for slow slip of a shallow subduction interface. *Science*, *348*(6235), 676–679. doi: 10.1126/science.aaa4242

Zha, X., Jia, Z., Dai, Z., & Lu, Z. (2019). The cause of the 2011 Hawthorne (Nevada) earthquake swarm constrained by seismic and InSAR methods. *Journal of Geodesy*, *93*(6), 899–909. doi: 10.1007/s00190-018-1212-5

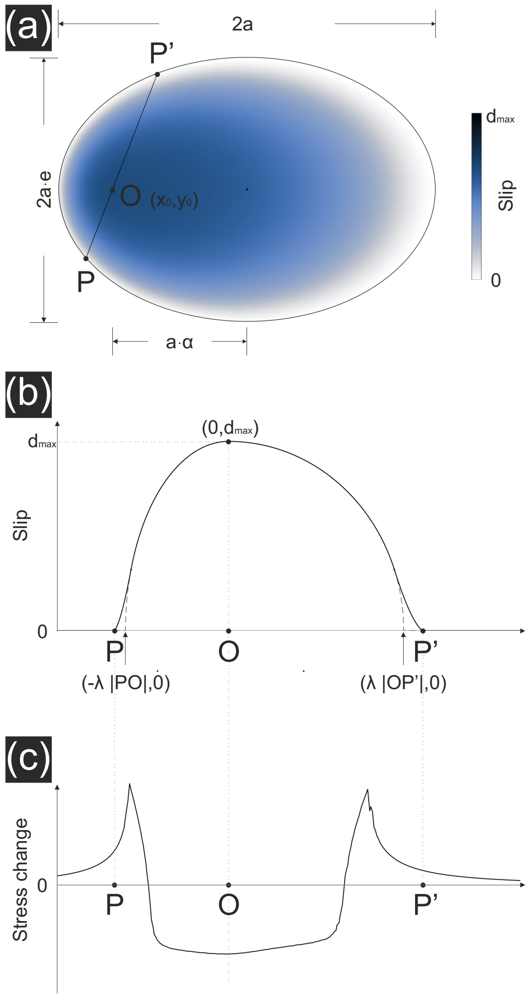

Figure 1. Parameters of the proposed slip model. Image (a) shows the 2d slip distribution, with an elliptical shape. The slip and stress changes along profile POP' are presented in images (b)-(c).

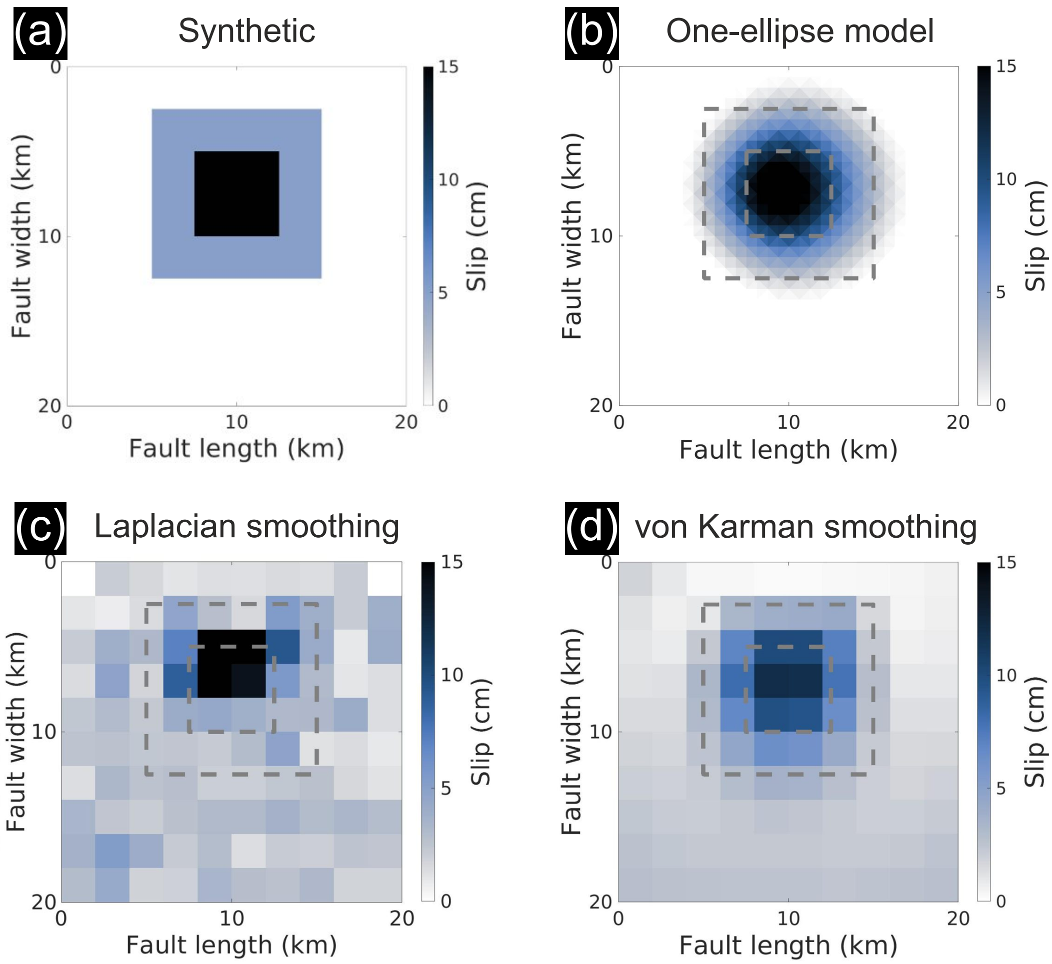

Figure 2. Synthetic and modeled fault slip distribution for a synthetic case. Image (a) shows the synthetic non-uniform slip distribution on a simulated fault plane. The black area is a 5km × 5km region with 15cm down-dip slip. The blue area is a 10km × 10km region with 5cm down-dip slip. No slip occurs in the white area. Images (b)-(d) are the inverted fault slip distribution based on the optimal model with maximum likelihood estimated by one-ellipse model (GICMo), Laplacian smoothing and von Karman smoothing (slipBERI). The dashed line in image (b)-(d) indicate the boundary of various slipping area in image (a).

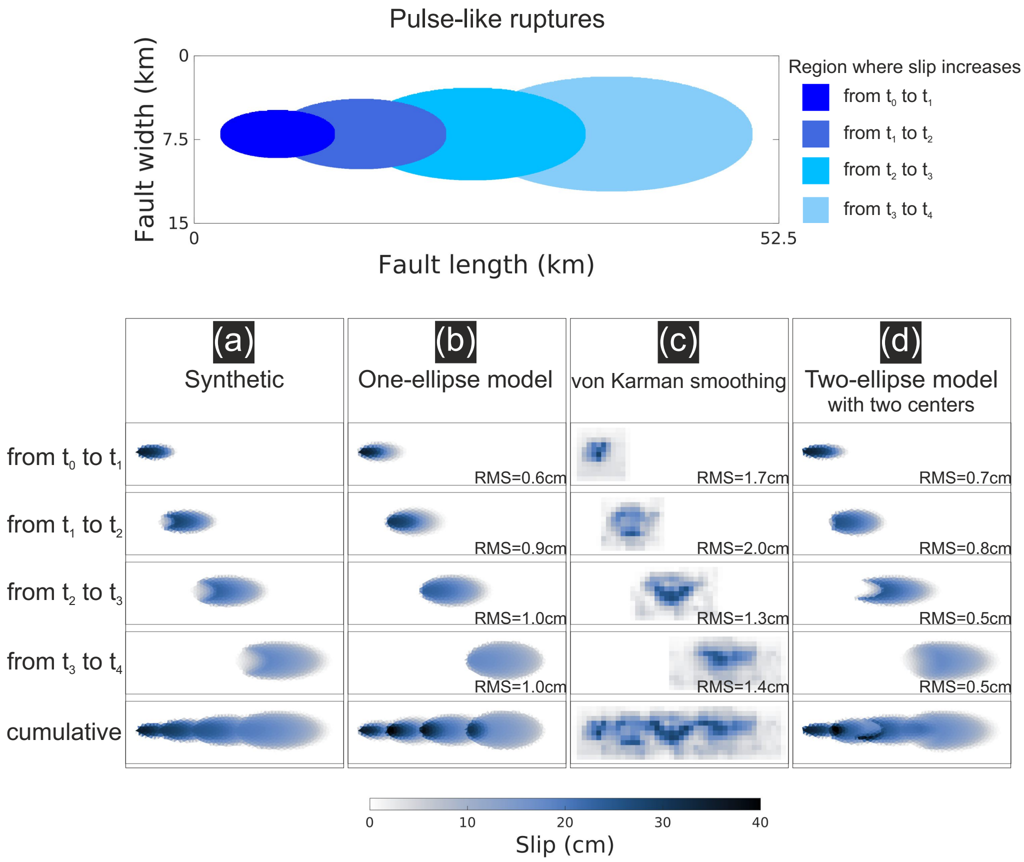

Figure 3. Synthetic and modeled fault slip distributions for synthetic case 2 (pulse-like ruptures). The top image is the conceptual diagram representing the growing cracks with the overlapping relationship. Images in column (a) show the synthetic slip increments. Images in columns (b)-(d) show the modeled slip distribution with various inversion methods: one-ellipse model (b), von Karman smoothing (c), and two-ellipse model with different centers (d), and the RMS of the slip residuals are shown at the bottom right.

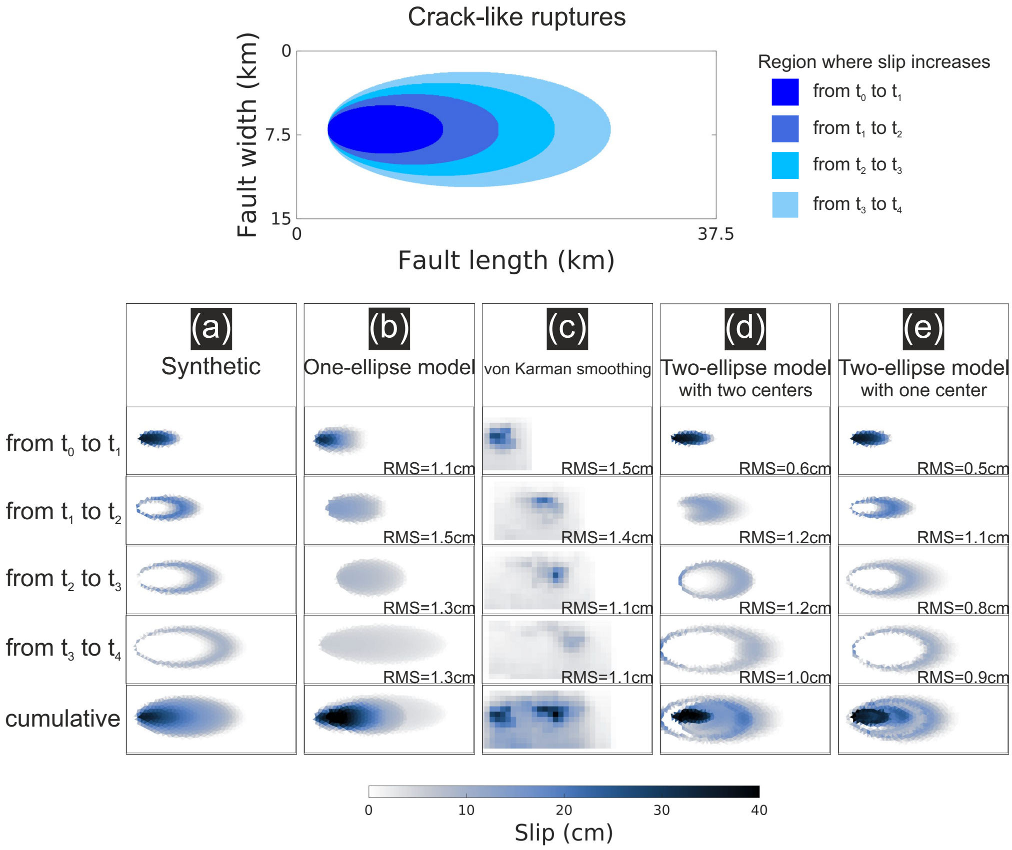

Figure 4. Synthetic and modeled fault slip distribution for synthetic case 2 (crack-like ruptures). The top image is the conceptual diagram presenting the growing cracks with the containing relationship. Images in column (a) show the synthetic slip increments. Images in columns (b)-(e) show the modeled slip distribution with various inversion methods: one-ellipse model (b), von Karman smoothing (c), two-ellipse model with different centers (d) and with the same center (e), and the RMS of the slip residuals are shown at the bottom right.

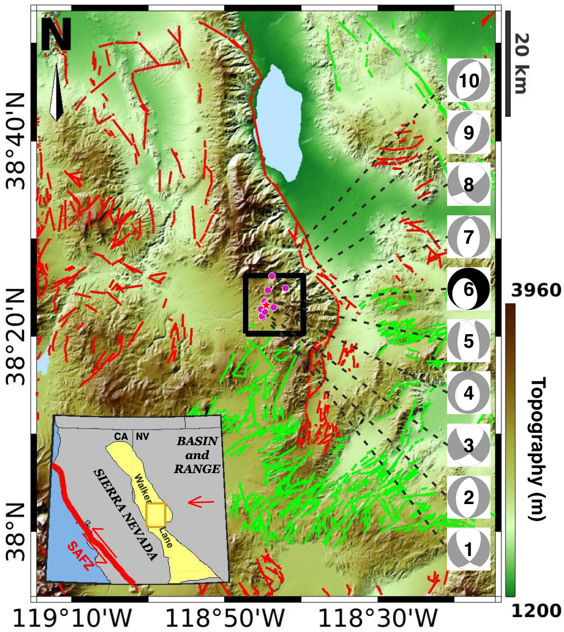

Figure 5. Tectonic settings for the 2011 Hawthorne seismic swarm. Image (a) shows the structural geologic environment of Walker Lane, located between the Sierra Nevada microplate and Basin and Range Province. It accommodates relative motion between the Pacific and North America. The brown rectangular box is the boundary of image (b), the central segment of Walker Lane. Image (b) shows the detailed tectonic settings for the 2011 Hawthorne seismic swarm, with topography as the base map. Normal and strike-slip faults are plotted as red and green lines. The beach balls on the right show the focal mechanism solutions provided by the Nevada Seismological Laboratory (Ichinose et al., 2003). Beach ball No.6 in black is the event with the largest magnitude, M4.6. Abbreviation: SAFZ, San Andreas Fault Zone

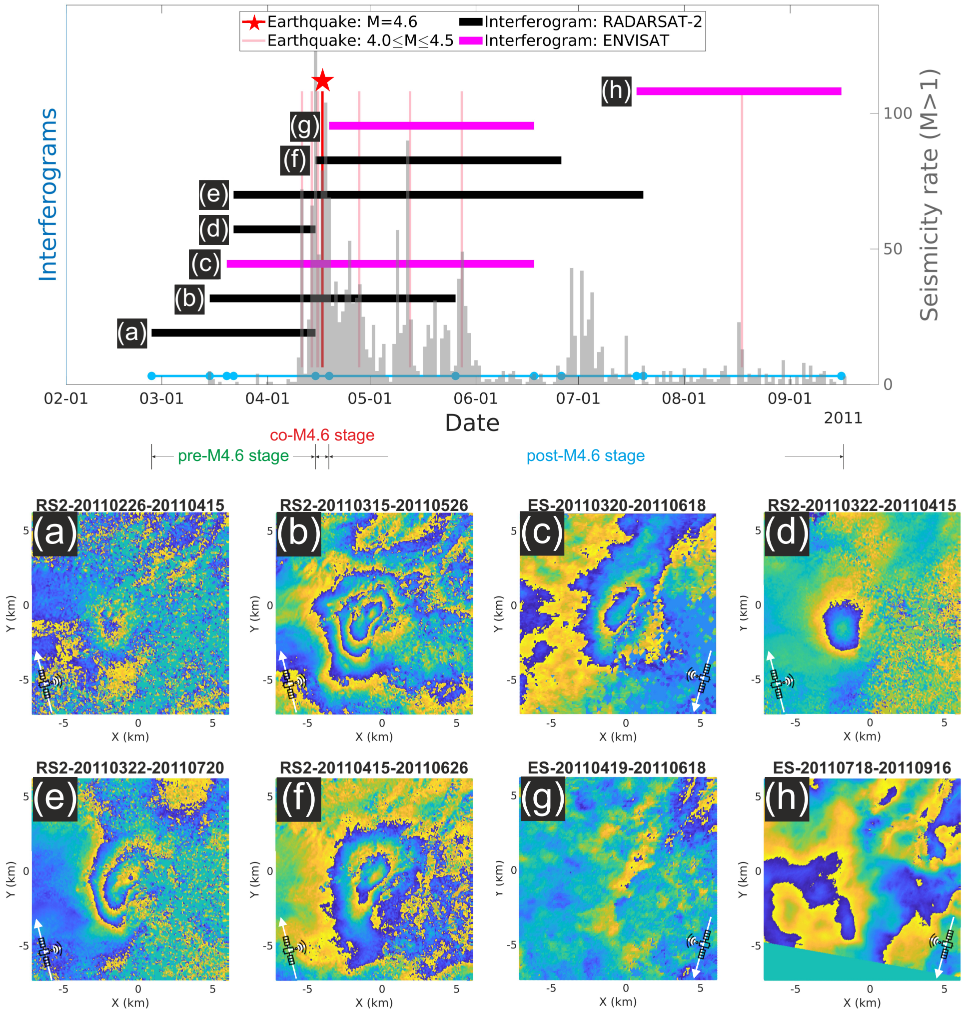

Figure 6. Surface displacement observations for the 2011 Hawthorne seismic swarm. In this research, the 2011 Hawthorne seismic swarm is divided into 3 stages with respect to the larges event, M4.6 on April 17 2011 (red star in the top image): pre-, co- and post-M4.6 event. The top image shows the time coverage of the interferograms (horizontal lines) over M≥4 events (vertical lines). Out of 8 interferograms (a)-(h), 5 are from RADARSAT-2 (black lines) and 3 from ENVISAT (magenta lines). For the blue line at the bottom, dots infer the 11 dates for the image sensing time in the interferograms. Images (a)-(g) show the observed wrapped phases of the interferograms capturing the surface deformation of the seismic swarm, while no clear deformation signal is detectable in image (h). The spatial reference point is [38.3875°N, 118.725°W].

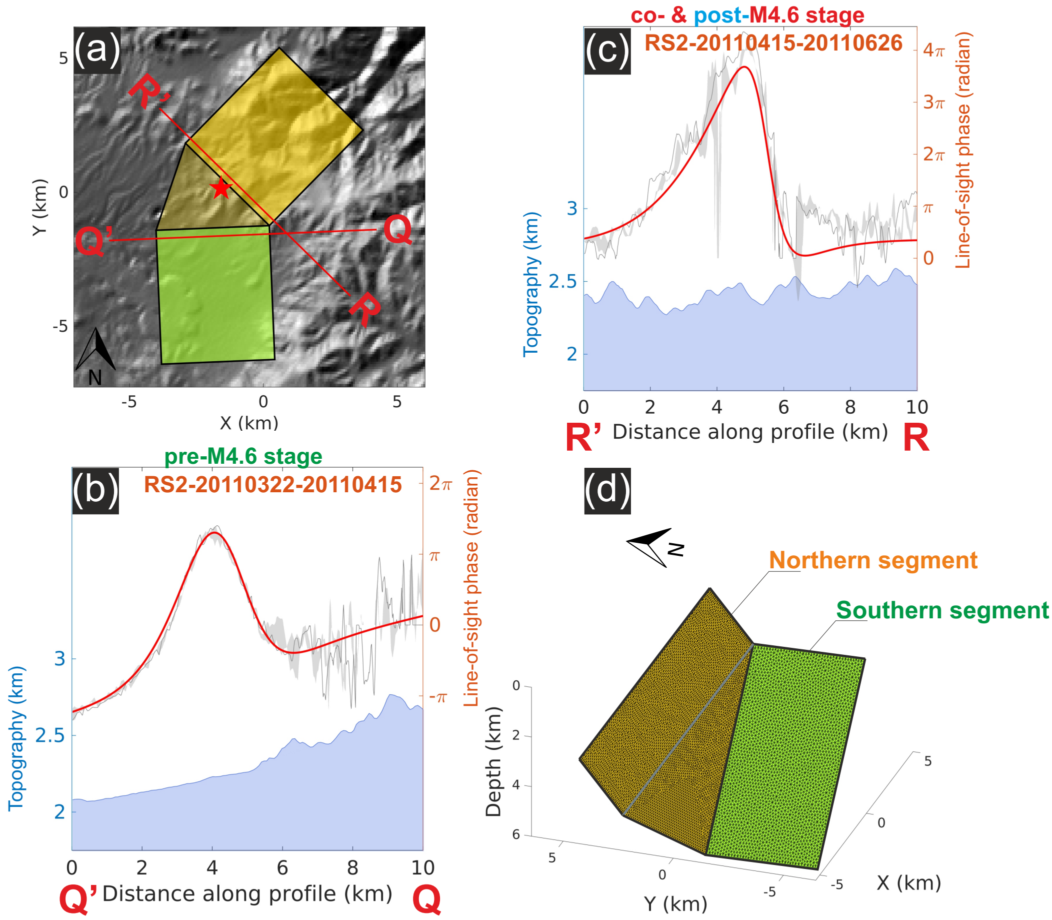

Figure 7. Fault geometry for the 2011 Hawthorne seismic swarm. Image (a) indicates the fault plane with uniform slip retrieved by WGBIS (Jiang & González, 2020) from the wrapped interferograms, and the modeled phase and phase residuals are shown in Figure S8. In image (a), the green rectangle indicates the southern subfault which is active during the pre-M4.6 stage, retrieved from RADARSAT-2 interferogram 2011/03/22-2011/04/15; yellow rectangle indicates the northern subfault which is active during the co- and post-M4.6 stages, retrieved from the RADARSAT-2 interferogram 2011/04/15-2011/06/26, and the yellow triangle indicates the joint fault connecting two rectangle subfaults. Profiles QQ' and RR' are perpendicular to two rectangle subfaults and the red star indicates the hypocentre of the M4.6 event. Images (b) and (c) show the observed and modeled phase along profiles QQ' and RR'. Image (d) shows the discretization of the fault geometry in image (a), where the triangular mesh is generated by FaultResampler (Barnhart & Lohman, 2010) and mesh2d (Engwirda, 2014).

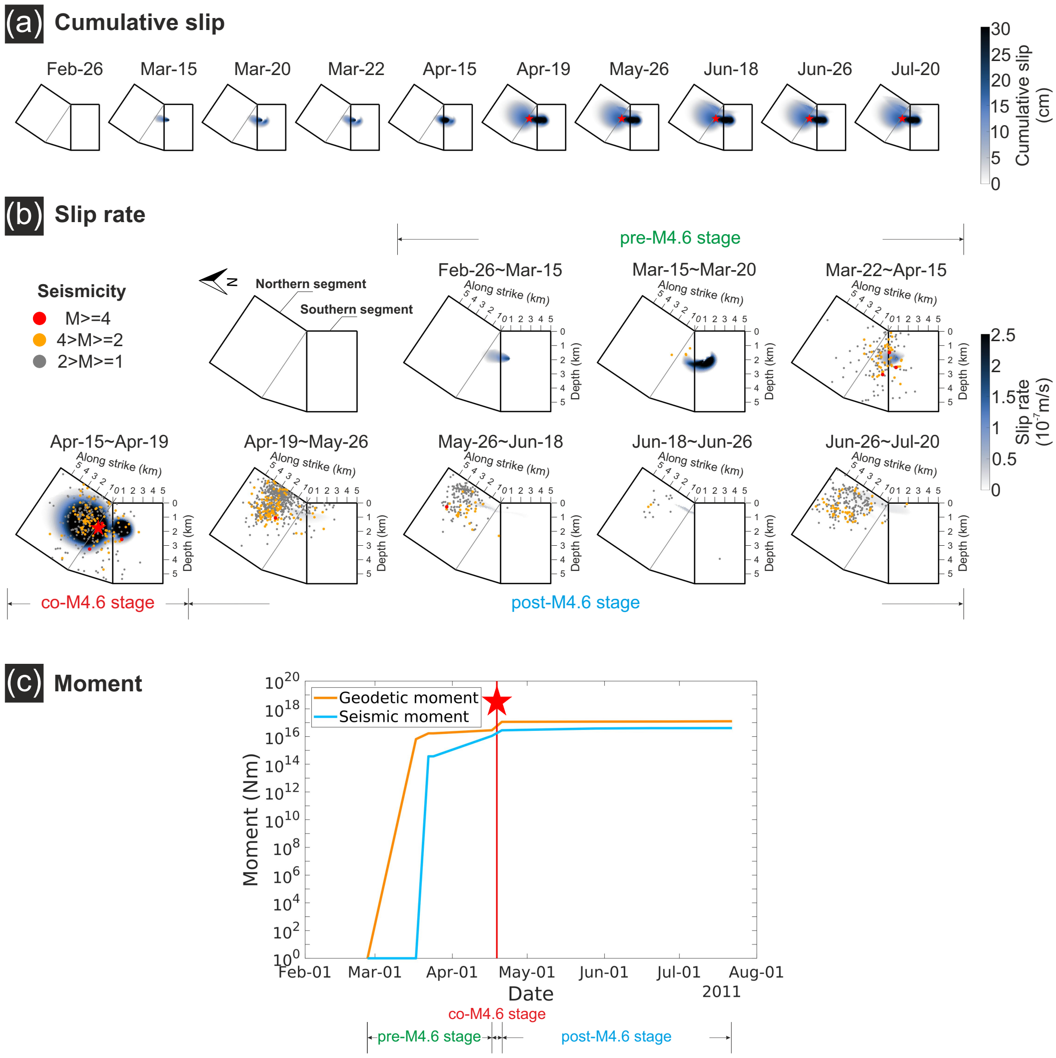

Figure 8. Slip evolution obtained from Time-GICMo inversion of pre-, co- and post-M4.6 stages during 2011 Hawthorne seismic swarm. Image (a) shows the accumulated slip at 10 dates, representing the acquisition time of images in Figures 6a to 6g. Image (b) presents the slip rate during the pre-, co- and post-M4.6 stages. In image (c), blue line shows the cumulative seismic moment based on the USGS earthquake catalog in the region [38.325°N ∼ 38.45°N, 118.675°W ∼ 118.775°W] (https://earthquake.usgs.gov/earthquakes/search/); orange line shows the cumulative geodetic moment, on the basis of estimated cumulative slip in image (a). A variable crustal shear modulus with depth is assumed based on the CRUST 1.0 model in the moment calculation.

Supporting Information for "Aseismic Fault Slip during a Shallow Normal-Faulting Seismic Swarm Constrained Using a Physically-Informed Geodetic Inversion Method"

Yu Jiang[1], Sergey V. Samsonov[2], and Pablo J. González[1,3]

[1]COMET, Dept. Earth, Ocean and Ecological Sciences, School of Environmental Sciences, University of Liverpool, Liverpool, L69 3BX, United Kingdom

[2]Canada Centre for Mapping and Earth Observation, Natural Resources Canada, 560 Rochester Street, Ottawa, ON K1S5K2, Canada

[3]Department of Life and Earth Sciences, Instituto de Productos Naturales y Agrobiología (IPNA-CSIC), 38206 La Laguna, Tenerife, Canary Islands, Spain

Contents of this file

1. Figures S1 to S10
2. Tables S1

Introduction This document contains supplementary figures and table. Figure S1 shows the observed and modelled InSAR phase for the synthetic case 1. Figures S2-S3 show the observed and modelled InSAR phase for synthetic case 2 (pulse-like ruptures). Figure S4-S5 show the observed and modelled InSAR phase for synthetic case 2 (crack-like ruptures). Figure S6 shows the wrapped and unwrapped InSAR phase for the descending ENVISAT interferogram. Figure S7 shows the estimation of the covariance function from the non-deformaed region. Figure S8 shows the inversion for two subfaults in the 2011 Hawthorne swarm, including the southern subfault in the pre-M4.6 stage, and the northern subfault during the co- and post-M4.6 stage. Figure S9 shows the modelled InSAR phases based on the fault geometry from nonlinear inversion (WGBIS). Figure S10 shows the degree of similarity between idealized one-ellipse crack model and published finite slip distribution datasets as a function of magnitudes. Table S1 summarized the parameters of slow slip listed in Section 5.2. For each event the table lists the event location, date, type and the reference from which the information was obtained.

References

Bletery, Q., & Nocquet, J. M. (2020). Slip bursts during coalescence of slow slip events in Cascadia. *Nature Communications*, *11*(1), 1–6. doi: 10.1038/s41467-020-15494-4

Cheloni, D., D'Agostino, N., Selvaggi, G., Avallone, A., Fornaro, G., Giuliani, R., . . . Tizzani, P. (2017). Aseismic transient during the 2010-2014 seismic swarm: Evidence for longer recurrence of M≥6.5 earthquakes in the Pollino gap (Southern Italy)? *Scientific Reports*, *7*(1), 1–10. doi: 10.1038/s41598-017-00649-z

De Barros, L., Cappa, F., Deschamps, A., & Dublanchet, P. (2020). Imbricated Aseismic Slip and Fluid Diffusion Drive a Seismic Swarm in the Corinth Gulf, Greece. *Geophysical Research Letters*, *47*(9). doi: 10.1029/2020GL087142

Guglielmi, Y., Cappa, F., Avouac, J. P., Henry, P., & Elsworth, D. (2015). Seismicity triggered by fluid injection-induced aseismic slip. *Science*, *348*(6240), 1224–1226. doi: 10.1126/science.aab0476

Hirose, H., & Obara, K. (2010). Recurrence behavior of short-term slow slip and correlated nonvolcanic tremor episodes in western Shikoku, southwest Japan. *Journal of Geophysical Research: Solid Earth*, *115*(B6), 0–21. doi: 10.1029/2008JB006050

Houston, H., Delbridge, B. G., Wech, A. G., & Creager, K. C. (2011). Rapid tremor reversals in Cascadia generated by a weakened plate interface. *Nature Geoscience*, *4*(6), 404–409. doi: 10.1038/ngeo1157

Hussain, E., Hooper, A., Wright, T. J., Walters, R. J., & Bekaert, D. P. (2016). Interseismic strain accumulation across the central North Anatolian Fault from iteratively unwrapped InSAR measurements. *Journal of Geophysical Research: Solid Earth*, *121*(12), 9000–9019. doi: 10.1002/2016JB013108

Jiang, Y., & González, P. J. (2020). Bayesian Inversion of Wrapped Satellite Interferometric Phase to Estimate Fault and Volcano Surface Ground Deformation Models. *Journal of Geophysical Research: Solid Earth*, *125*(5). doi: 10.1029/2019JB018313

Johanson, I. A., & Bürgmann, R. (2005). Creep and quakes on the northern transition zone of the San Andreas fault from GPS and InSAR data. *Geophysical Research Letters*, *32*(14), 1–5. doi: 10.1029/2005GL023150

Jolivet, R., Lasserre, C., Doin, M. P., Guillaso, S., Peltzer, G., Dailu, R., ... Xu, X. (2012). Shallow creep on the Haiyuan Fault (Gansu, China) revealed by SAR Interferometry. *Journal of Geophysical Research: Solid Earth*, *117*(B6), 6401. doi: 10.1029/2011JB008732

Khoshmanesh, M., Shirzaei, M., & Nadeau, R. M. (2015). Time-dependent model of aseismic slip on the central San Andreas Fault from InSAR time series and repeating earthquakes. *Journal of Geophysical Research: Solid Earth*, *120*(9), 6658–6679. doi: 10.1002/2015JB012039

Kyriakopoulos, C., Chini, M., Bignami, C., Stramondo, S., Ganas, A., Kolligri, M., & Moshou, A. (2013). Monthly migration of a tectonic seismic swarm detected by DInSAR: Southwest Peloponnese, Greece. *Geophysical Journal International*, *194*(3), 1302–1309. doi: 10.1093/gji/ggt196

López-Comino, J. A., Stich, D., Morales, J., & Ferreira, A. M. (2016). Resolution of rupture directivity in weak events: 1-D versus 2-D source parameterizations for the 2011, Mw 4.6 and 5.2 Lorca earthquakes, Spain. *Journal of Geophysical Research: Solid Earth*, *121*(9), 6608–6626. doi: 10.1002/2016JB013227

Mesimeri, M., & Karakostas, V. (2018). Repeating earthquakes in western Corinth Gulf (Greece): Implications for aseismic slip near locked faults. *Geophysical Journal International*, *215*(1), 659–676. doi: 10.1093/gji/ggy301

Nadeau, R. M., & McEvilly, T. V. (1999). Fault slip rates at depth from recurrence intervals of repeating microearthquakes. *Science*, *285*(5428), 718–721. doi: 10.1126/science.285.5428.718

Ozawa, S., Yarai, H., & Kobayashi, T. (2019). Recovery of the recurrence interval of Boso slow slip events in Japan. *Earth, Planets and Space*, *71*(1), 1–8. doi: 10.1186/s40623-019-1058-y

Passarelli, L., Rivalta, E., Jónsson, S., Hensch, M., Metzger, S., Jakobsdóttir, S. S., ... Dahm, T. (2018). Scaling and spatial complementarity of tectonic earthquake swarms. *Earth and Planetary Science Letters*, *482*, 62–70. doi: 10.1016/j.epsl.2017.10.052

Rousset, B., Fu, Y., Bartlow, N., & Bürgmann, R. (2019). Weeks-Long and Years-Long Slow Slip and Tectonic Tremor Episodes on the South Central Alaska Megathrust.

Journal of Geophysical Research: Solid Earth, *124*(12), 13392–13403. doi: 10.1029/2019JB018724

Schmidt, D. A., Bürgmann, R., Nadeau, R. M., & D'Alessio, M. (2005). Distribution of aseismic slip rate on the Hayward fault inferred from seismic and geodetic data. *Journal of Geophysical Research: Solid Earth*, *110*(B8), 1–15. doi: 10.1029/2004JB003397

Scott, C., Bunds, M., Shirzaei, M., & Toke, N. (2020). Creep Along the Central San Andreas Fault From Surface Fractures, Topographic Differencing, and InSAR. *Journal of Geophysical Research: Solid Earth*, *125*(10), e2020JB019762. doi: 10.1029/2020JB019762

Song, X., Jiang, Y., Shan, X., Gong, W., & Qu, C. (2019). A Fine Velocity and Strain Rate Field of Present-Day Crustal Motion of the Northeastern Tibetan Plateau Inverted Jointly by InSAR and GPS. *Remote Sensing 2019, Vol. 11, Page 435*, *11*(4), 435. doi: 10.3390/RS11040435

Turner, R. C., Nadeau, R. M., & Bürgmann, R. (2013). Aseismic slip and fault interaction from repeating earthquakes in the Loma Prieta aftershock zone. *Geophysical Research Letters*, *40*(6), 1079–1083. doi: 10.1002/grl.50212

Wech, A. G., Creager, K. C., & Melbourne, T. I. (2009). Seismic and geodetic constraints on Cascadia slow slip. *Journal of Geophysical Research: Solid Earth*, *114*(10). doi: 10.1029/2008JB006090

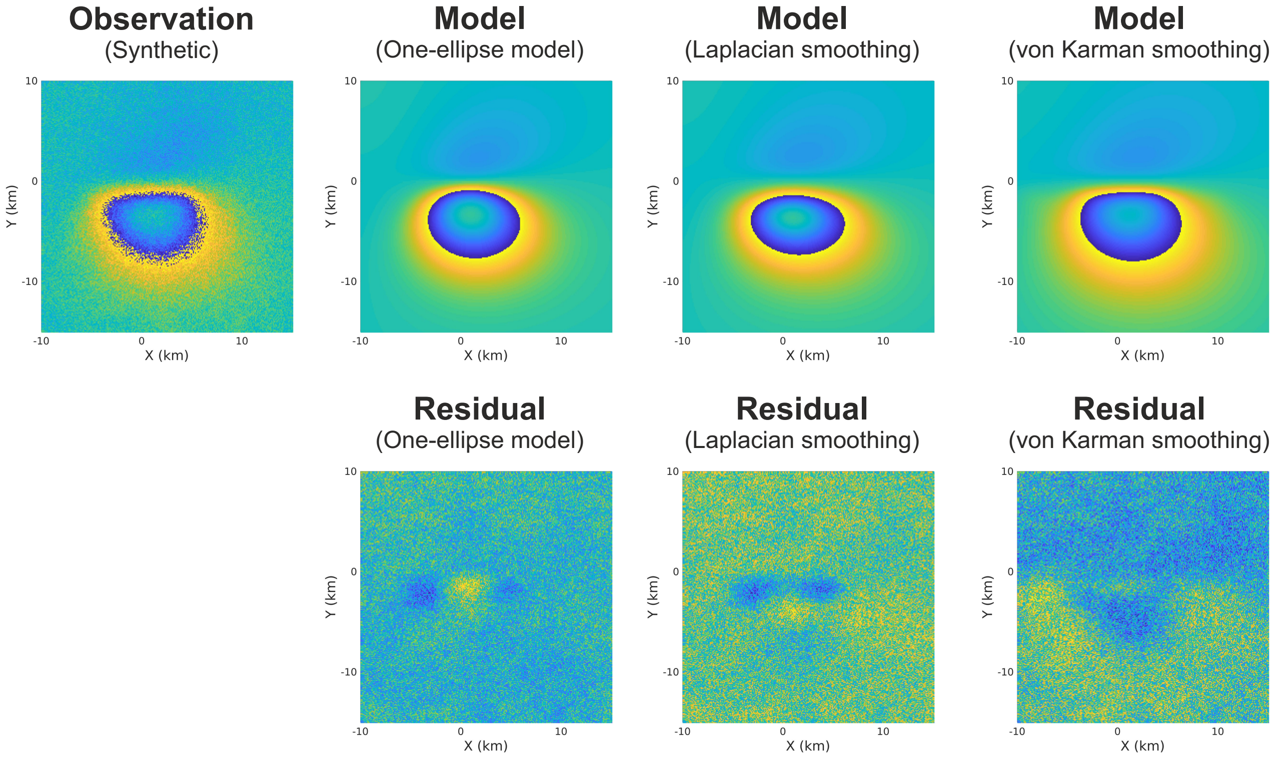

Figure S1. Synthetic and modeled InSAR phases for a synthetic case. The observed InSAR phase is forward calculated on the basis of the synthetic fault slip in Figure 2(a). The modelled InSAR phases are forward calculated on the basis of modelled slip distributions in Figure 2(b)-(c) estimated by one-ellipse model and laplacian smoothing. The bottom images show the residual phases.

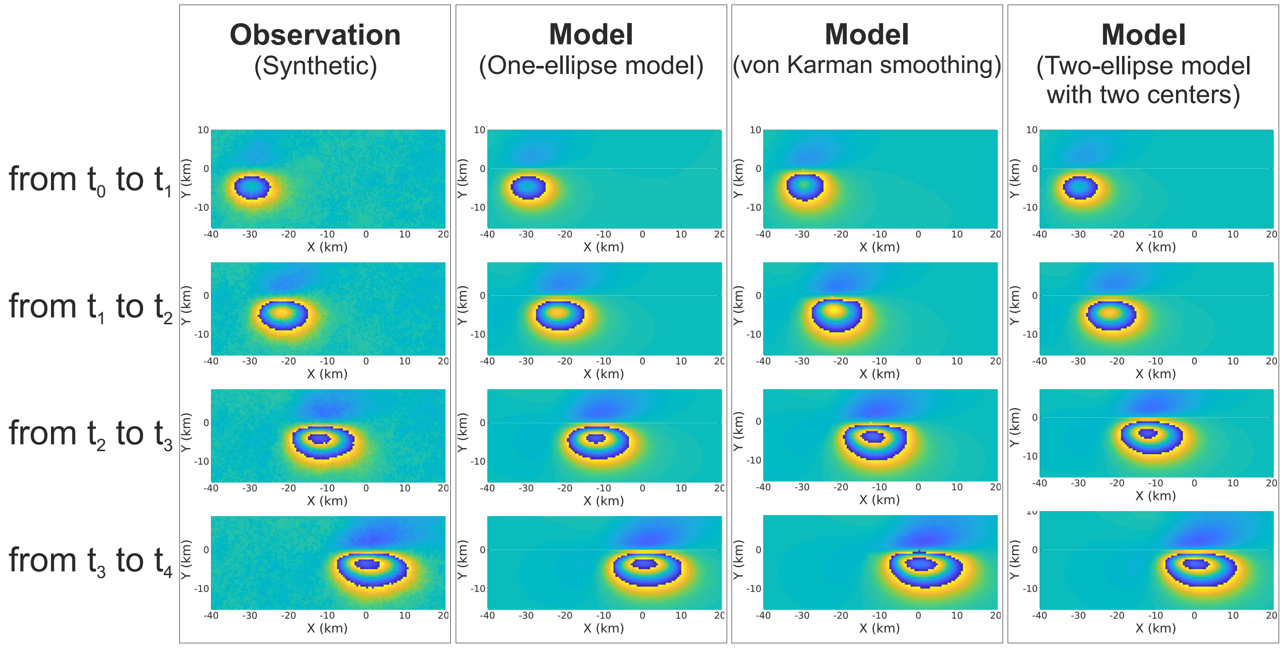

Figure S2. Synthetic and modeled InSAR phases for synthetic case 2 (pulse-like ruptures). The observed InSAR phase is forward calculated on the basis of the synthetic fault slip in Figure 3(a). The modelled InSAR phases are forward calculated on the basis of modelled slip distributions in Figure 3(b)-(d) with various methods: one-ellipse model, von Karman smoothing, and two-ellipse model with different centers.

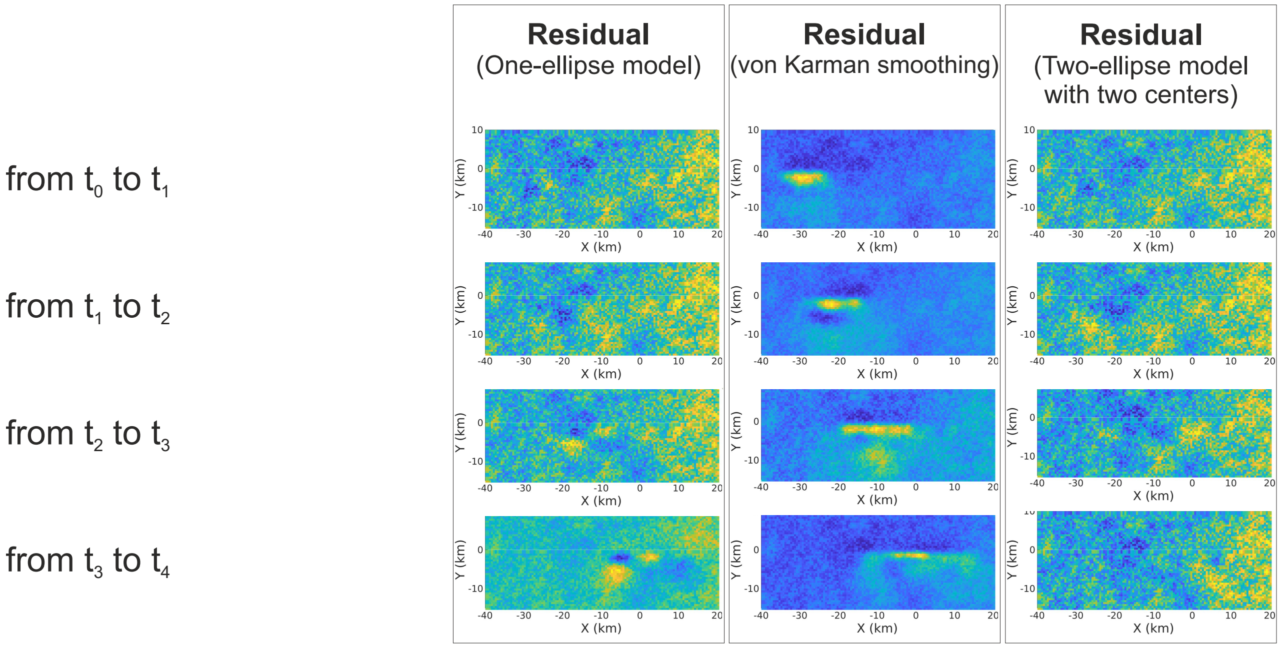

Figure S3. Residual InSAR phases for synthetic case 2 (pulse-like ruptures).

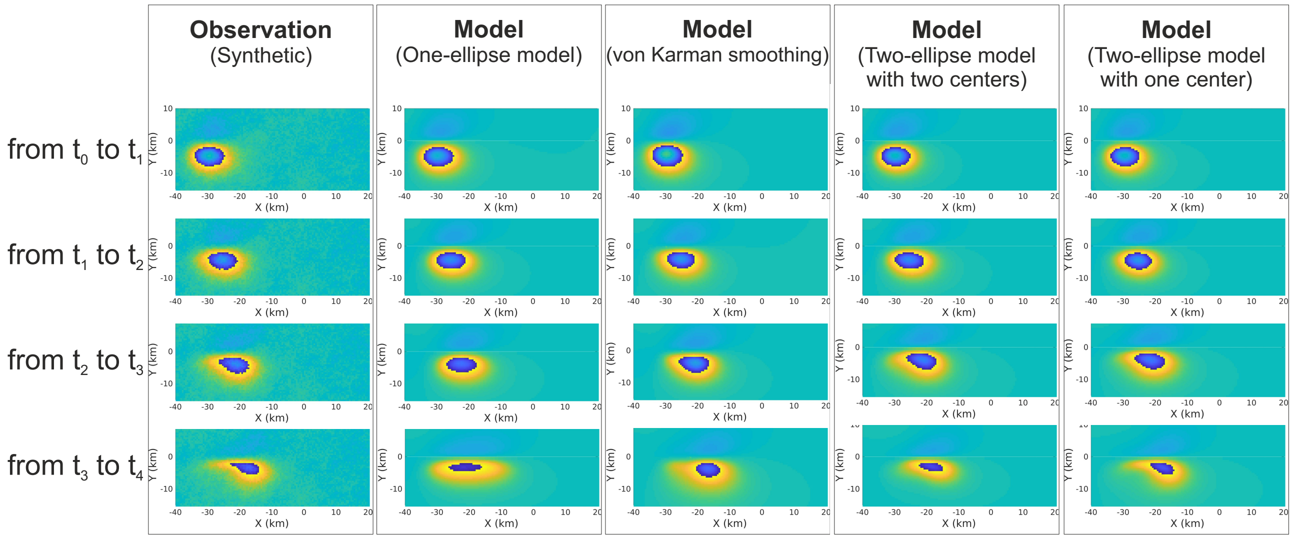

Figure S4. Synthetic and modeled InSAR phases for synthetic case 2 (crack-like ruptures). The observed InSAR phase is forward calculated on the basis of the synthetic fault slip in Figure 4(a). The modelled InSAR phases are forward calculated on the basis of modelled slip distributions in Figure 4(b)-(e) with various methods: one-ellipse model, von Karman smoothing, and two-ellipse model with different centers and with the same center.

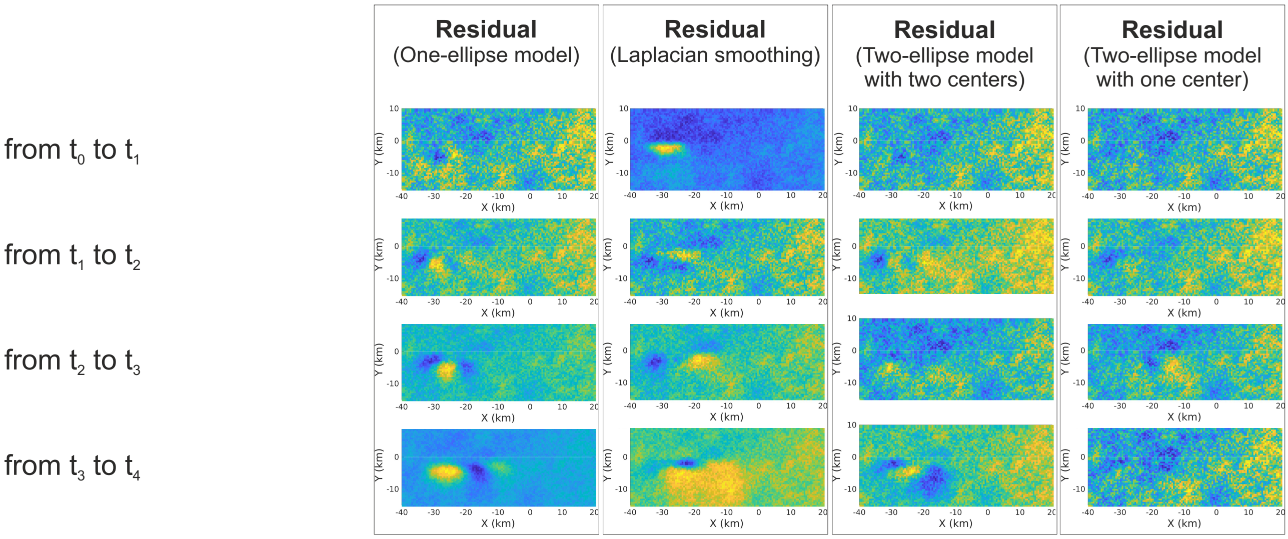

Figure S5. Residual InSAR phases for synthetic case 2 (crack-like ruptures).

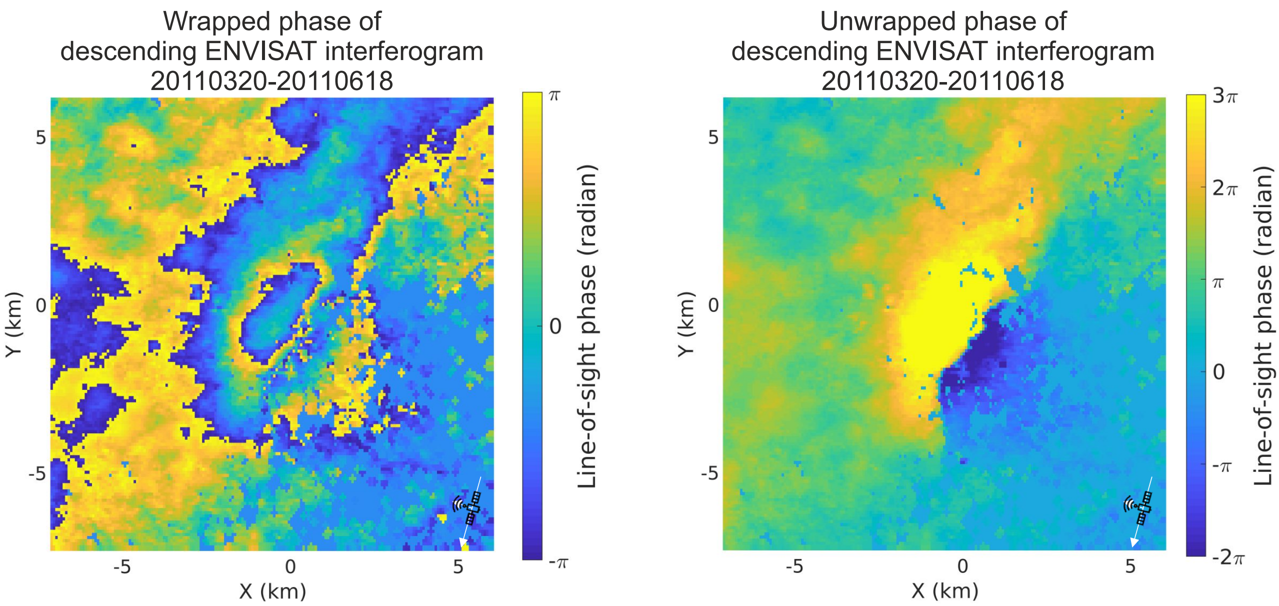

Figure S6. Wrapped and unwrapped phase in the descending ENVISAT interferogram 2011/03/20-2011/06/18.

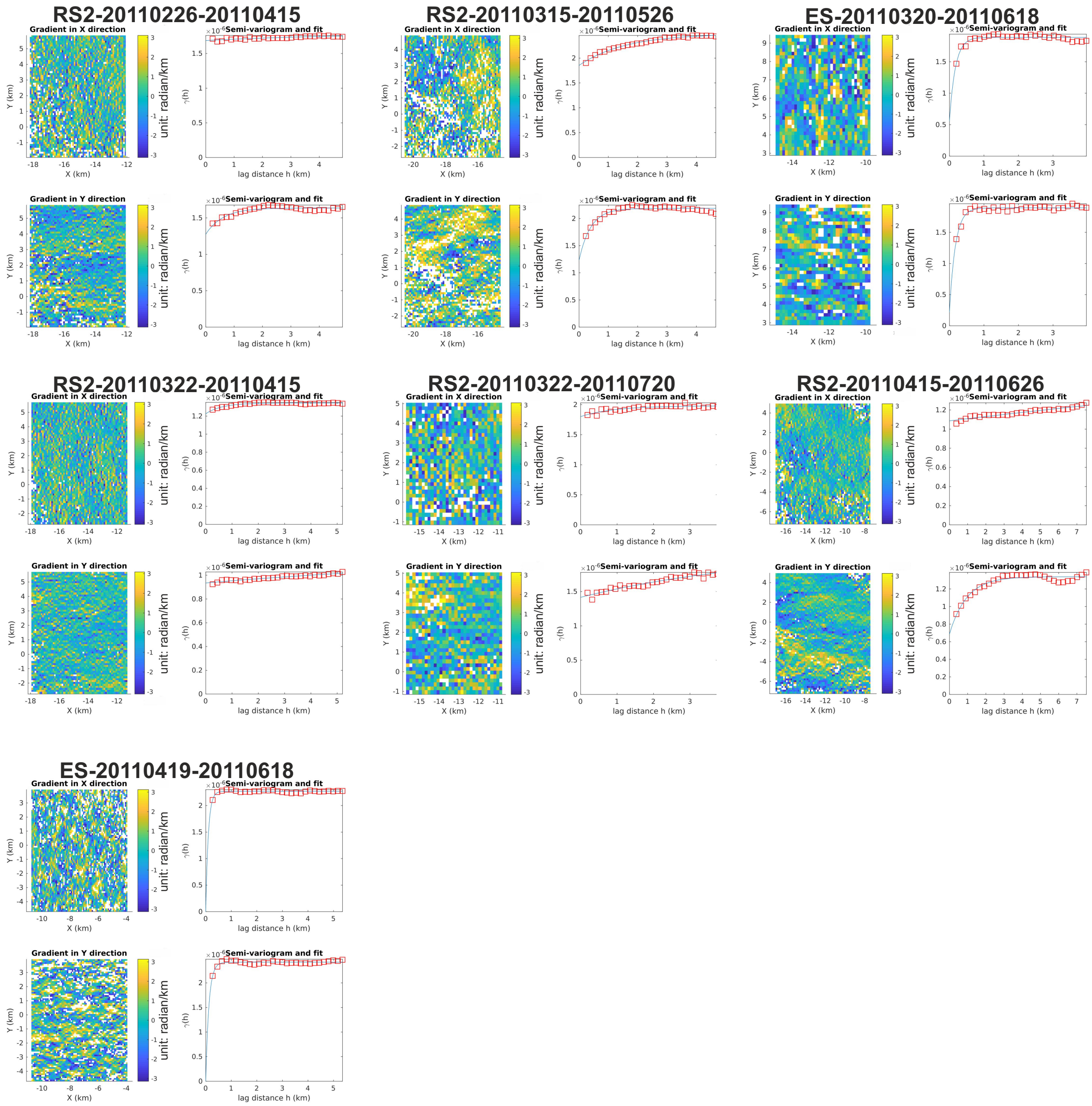

Figure S7. Covariance function estimation from the phase in the nondeformed region of the interferograms used in the 2011 Hawthorne seismic swarm. The chosen region for covariance estimation is the undeformed region. For each panel, images on the left are the downsampled phase gradients in X-direction and Y-direction; images on the right side show the experimental (rectangular) and theoretical (solid line) semivariograms are shown for phase gradients in X-direction and Y-direction, estimating from the downsampled phase gradients according to equation 9 in Jiang and González (2020).

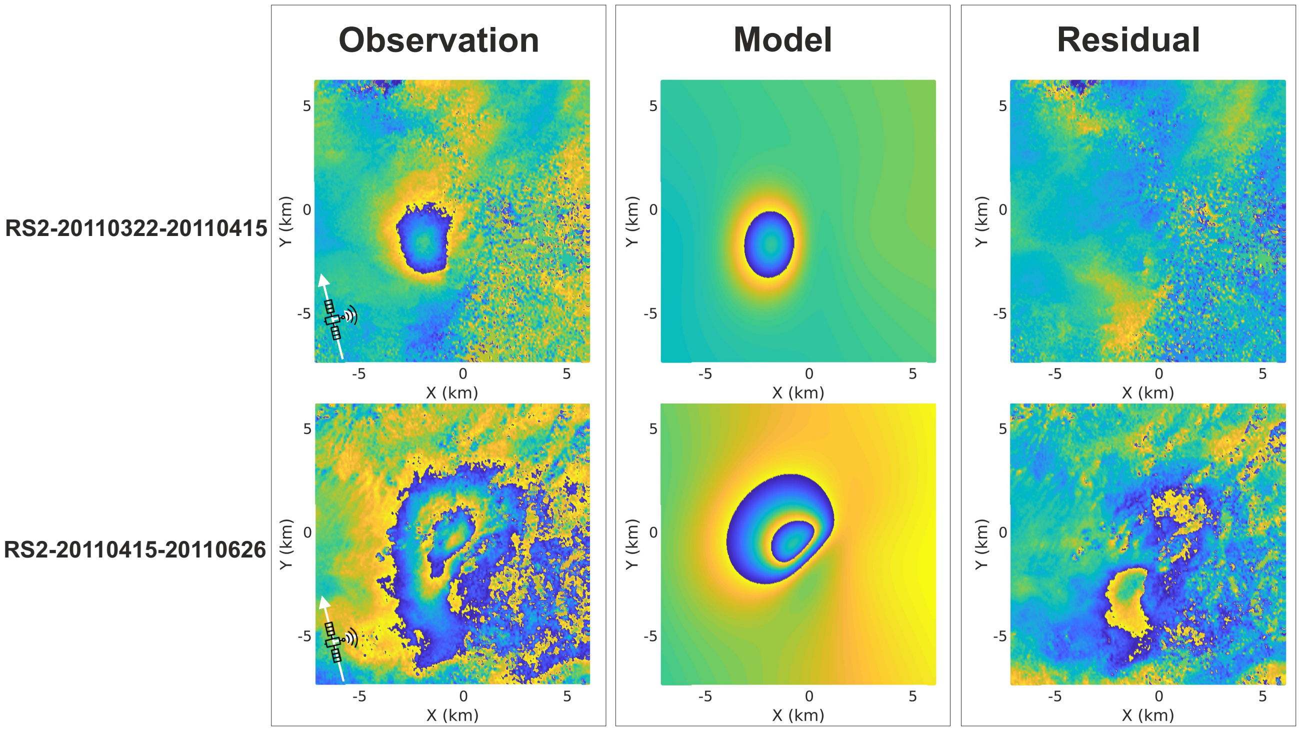

Figure S8. Observed and modeled InSAR displacements with WGBIS. Images at the top row show the observed, modelled and residual phases for ascending RADARSAT-2 interferogram 2011/03/22-2011/04/15, covering the pre-M4.6 stage of the 2011 Hawthorne swarm. Images at the bottom row show the observed, modelled and residual phases for ascending RADARSAT-2 interferogram 2011/04/15-2011/06/26, covering the co- and post-M4.6 stage of the 2011 Hawthorne swarm.

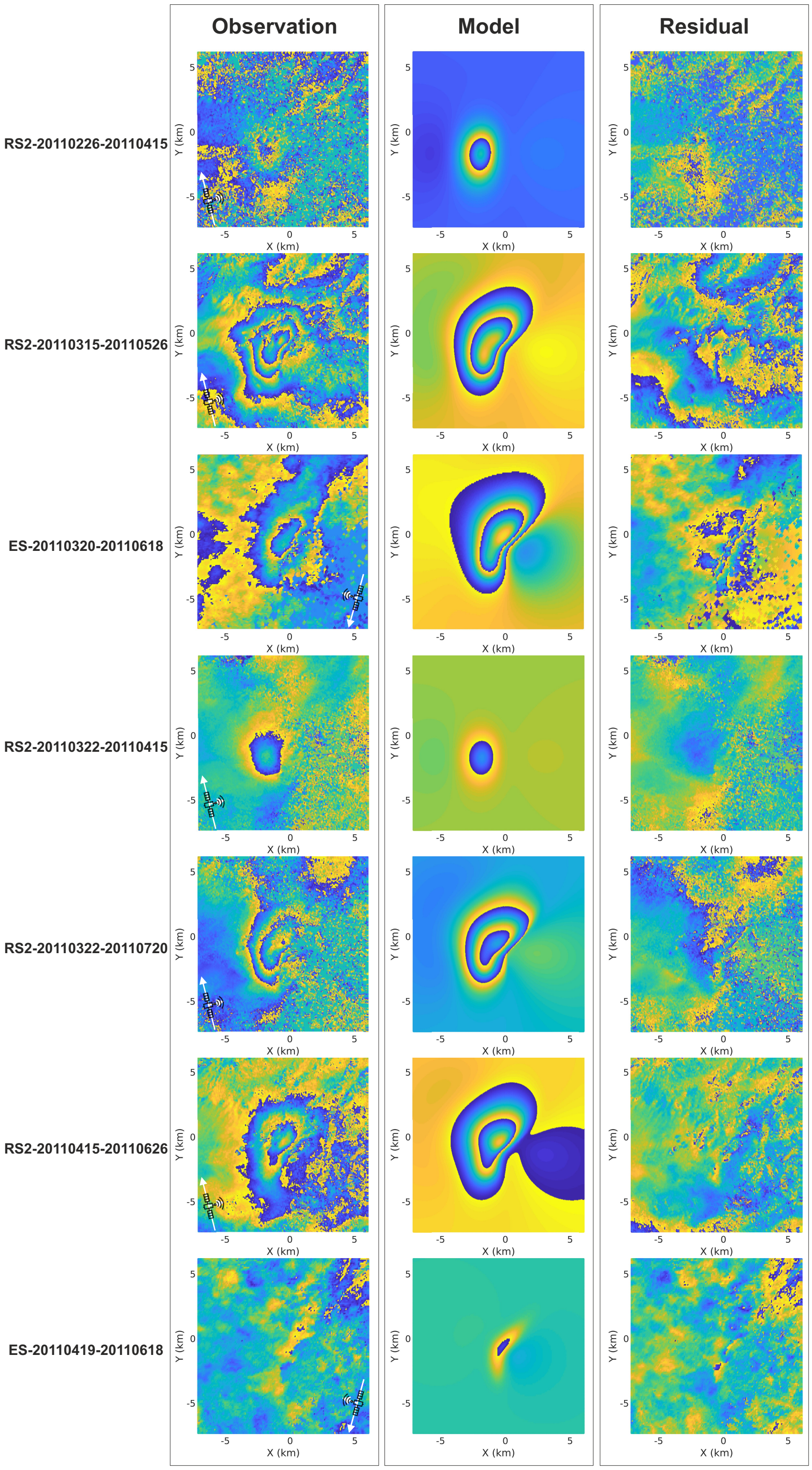

Figure S9. Observed and modeled InSAR displacements of the 2011 Hawthorne swarm by using the discretized fault geometry retrieved from WGBIS. The modelled phases are forward calculated on the basis of the modelled slip distributions in Figure 8(a) and discretized fault geometry in Figure 7(d).

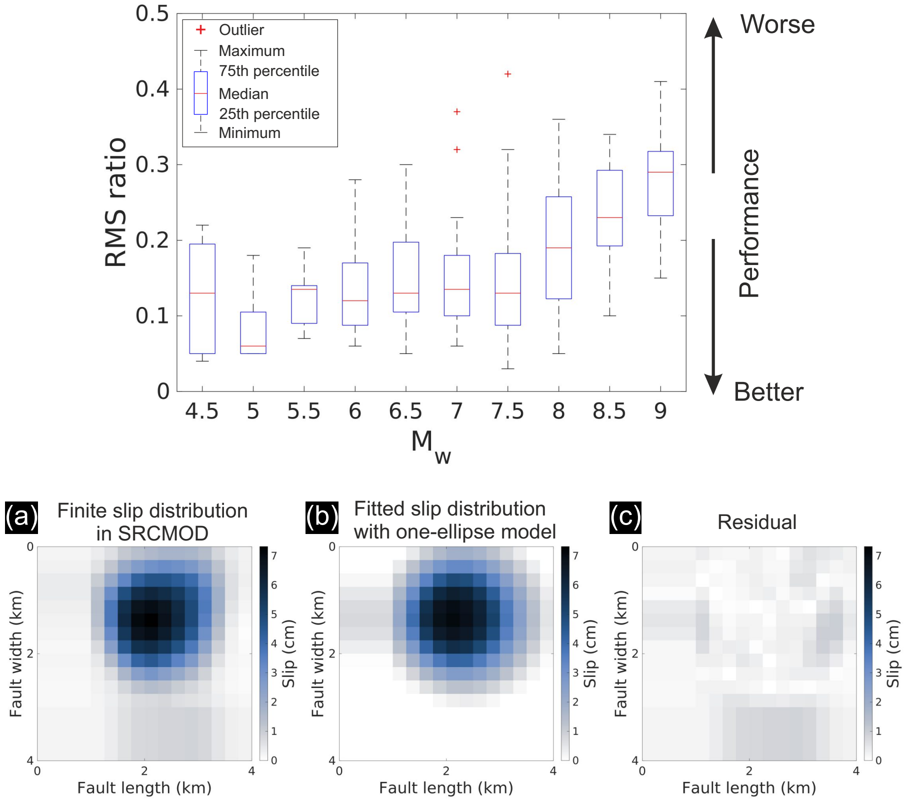

Figure S10. This figure shows the degree of similarity between idealized one-ellipse crack model and published finite slip distribution datasets as a function of magnitudes. A one-ellipse crack model is used to approximate the finite slip distributions in SRCMOD for each dataset containing 25 fault patches or more. We obtain a best fitting model for each selected dataset. We estimate the misfit between the best fitting crack model and SRCMOD estimated fault slips as the RMS error. Top image presents the ratio between RMS and peak slip for each case in the SRCMOD dataset. Lower values of the ratio indicate better agreement. Bottom images present an example for comparison of a SRCMOD event (2011 M_w 4.6 Lorca earthquakes, Spain, López-Comino et al. (2016)) and its best-fitting ellipse model.

Table S1. Parameters of slow slip phenomena considered in this study

Name	Type	Value	Source location and date	(Reference)
Peak slip rate (cm/day)	SSE	0.27	[124°W, 49°N], Cascadia subduction zone, 2013	(Bletery & Nocquet, 2020)
Peak slip rate (cm/day)	SSE	0.3	[149°W, 62°N], Central Alaska Megathrust, 2010	(Rousset et al., 2019)
Peak slip rate (cm/day)	SSE	0.6-1.1	[132.5°E, 33.5°N], Western Shikoku, Japan, 2002-2007	(Hirose & Obara, 2010)
Peak slip rate (cm/day)	SSE	1.1-2.8	[141°E, 35°N], Boso peninsula, Japan, 1996-2018	(Ozawa et al., 2019)
Peak slip rate (cm/day)	Seismic swarm	0.26	[22°E, 37.24°N], Peloponnese peninsula, Greece, 2011	(Kyriakopoulos et al., 2013)
Peak slip rate (cm/day)	Fluid injection experiments	35	France, ?	(Guglielmi et al., 2015)
Peak slip rate (cm/day)	Fault creep	0.001	[122.25°W, 37.5°N], Hayward fault, USA, 1992-2000	(Schmidt et al., 2005)
Peak slip rate (cm/day)	Fault creep	0.001	[105°E, 36.5°N], Haiyuan fault, China, 2003-2010	(Jolivet et al., 2012); (Song et al., 2019)
Peak slip rate (cm/day)	Fault creep	0.002	[32.5°E, 40.75°N], North Anatolia fault, Turkey, 2003-2010	(Hussain et al., 2016)
Peak slip rate (cm/day)	Fault creep	0.005	[121.4°W, 36.8°N], San Anreas fault, USA, 2001-2003	(Johanson & Bürgmann, 2005)
Peak slip rate (cm/day)	Fault creep	0.008	[121°W, 36.2°N], Central segment of San Andreas fault, USA, 2003-2011	(Khoshmanesh et al., 2015)
Peak slip rate (cm/day)	Fault creep	0.007	[121°W, 36.4°N], Central segment of San Andreas fault, USA, 2012-2020	(Scott et al., 2020)
Average rate of slip increment (cm/day)	Seismic swarm	0.1	[16°E, 39.9°N], Pollino gap, Southern Italy, 2010-2014	(Cheloni et al., 2017)
Average rate of slip increment (cm/day)	Repeating earthquakes	0.01	[116.7°W, 36.7°N], San Andreas fault, USA, 1994	(Nadeau & McEvilly, 1999)
Average rate of slip increment (cm/day)	Repeating earthquakes	0.003	[121.6°W, 36.8°N], San Anreas fault, USA, 2003-2006	(Turner et al., 2013)
Average rate of slip increment (cm/day)	Repeating earthquakes	0.0006	[22°E, 38.4°N], Corinth Gulf, Greece, 2008-2014	(Mesimeri & Karakostas, 2018)
Migration velocity (km/day)	SSE	$\sim$10	[132.5°E, 33.5°N], Western Shikoku, Japan, 2002-2007	(Hirose & Obara, 2010)
Migration velocity (km/day)	ETS	$\sim$10	[123.5°W, 48.5°N], Cascadia subduction zone, 2004-2008	(Wech et al., 2009)
Migration velocity (km/day)	RTR	160-400	[123°W, 48°N], Cascadia subduction zone, 2004-2009	(Houston et al., 2011)
Migration velocity (km/day)	Seismic swarm	0.5-14	[18.6°W, 66.3°N], North Iceland, 1997-2015	(Passarelli et al., 2018)
Migration velocity (km/day)	Seismic swarm	2-10	[22°E, 38.4°N], Corinth Gulf, Greece, 2015	(De Barros et al., 2020)